Journal of Computational Physics 228 (2009) 7426–7451

Contents lists available at ScienceDirect

Journal of Computational Physics

journal homepage: www.elsevier.com/locate/jcp

Compact Accurately Boundary-Adjusting high-REsolution Technique for fluid dynamics

S.A. Karabasov [a,*], V.M. Goloviznin [b]

[a] Cambridge University, Engineering Department, Whittle Laboratory, 1J.J. Thompson Avenue, Cambridge CB3 0DY, United Kingdom
[b] Mathematical Modelling Division, Moscow Institute of Nuclear Safety, 52B. Tulskaya, Moscow 113191, Russia

ARTICLE INFO

Article history:
Received 9 October 2008
Received in revised form 22 June 2009
Accepted 30 June 2009
Available online 4 July 2009

Keywords:
Advection schemes
Hyperbolic equations
Quasi-linear conservation laws
Computational fluid dynamics

ABSTRACT

A novel high-resolution numerical method is presented for one-dimensional hyperbolic problems based on the extension of the original Upwind Leapfrog scheme to quasi-linear conservation laws. The method is second-order accurate on non-uniform grids in space and time, has a very small dispersion error and computational stencil defined within one space–time cell. For shock-capturing, the scheme is equipped with a conservative non-linear correction procedure which is directly based on the maximum principle. Plentiful numerical examples are provided for linear advection, quasi-linear scalar hyperbolic conservation laws and gas dynamics and comparisons with other computational methods in the literature are discussed.

1. Introduction

The solution of unsteady fluid dynamics problems has been a challenge for numerical methods in computational fluid dynamics (CFD) for decades, e.g. [25,13]. Among other classes of high-resolution methods, Flux Corrected Transport (FCT) and Total Variation Diminishing (TVD) schemes [2,12] have been an important class of numerical methods used for the solution of "convection-dominated" problems. The development of TVD or FCT schemes has been based on a few important ideas how to deal with the well-known dispersion and dissipation problems of Eulerian schemes. One of these ideas, after A. Harten, is the introduction of anti-diffusion fluxes to an original dissipative scheme with low dispersion, e.g. the first-order Godunov scheme [6], in order to reduce its dissipation in such a way to retain the boundness of the solution [19,35]. The alternative approach is to start with a less dissipative but dispersive scheme, e.g. second-order central finite-differences, and then use diffusion fluxes with non-linear flux limiters to reduce the dispersion error (e.g. [13,15]). High-order extensions of original FCT/TVD methods are used to achieve a more delicate balance between the dispersion and dissipation error. A standing alone subset of high-order methods is (Weighted) Essentially Non-Oscillatory schemes based on a solution-dependent stencil that is composed of high-order differences based on the minimum local variation [21,28]. Another example of upgrading high-resolution conservative methods to a high-order includes Discontinuous Galerkin (DG) methods [3,22,24]. Unlike finite-difference schemes DG is not based on extending the spatial stencil in space but uses additional degrees of freedom, i.e., higher-order moments of the solution, within a compact finite-element cell.

The cost and complexity of the high-order schemes is considerably higher in comparison to the standard second ('low') order TVD/FCT schemes. Nevertheless, the price for using high-order non-oscillatory schemes is accepted by the computational community for the problems where the standard 'low'-order methods require too fine grid to resolve short wave lengths without considerable dissipation and dispersion errors. Moreover, the fact that the standard 'low'-order shock-cap-

* Corresponding author.
E-mail addresses: sak36@eng.cam.ac.uk (S.A. Karabasov), gol@ibrae.ac.ru (V.M. Goloviznin).

0021-9991/$ - see front matter © 2009 Elsevier Inc. All rights reserved.
doi:10.1016/j.jcp.2009.06.037

turing schemes are not suitable for linear wave computations even poses a question whether second-order schemes are in general viable to use for flow problems which are sensitive to linear wave effects.

Our goal in the present publication is to demonstrate that second-order finite-difference algorithms can still be very efficient for a wide range of CFD problems. We are going to achieve this goal by introducing and promoting for CFD a new conservative finite-difference method, called Compact Accurately Boundary-Adjusting high-REsolution Technique (CABARET). CABARET is based on a novel compact formulation of the second-order Upwind Leapfrog (UL) scheme [7,8,16] by introducing separate conservation and flux variables. The independency of the conservation and flux variables is one of the key features of the new method. Another distinct feature of CABARET in comparison with the majority of high-resolution schemes, excluding Lax–Wendroff-type methods, is that it is fully discrete in space and time. The CABARET scheme is made non-oscillatory by applying a non-linear flux correction algorithm to the compact formulation of the UL scheme. The flux correction is directly based on the maximum principle. In comparison with many high-resolution schemes based on the anti-diffusion/diffusion flux approaches, in CABARET the non-linear flux correction is applied to the originally fully non-dissipative and low-dispersive scheme.

The paper is organised as follows. In Section 2, CABARET is introduced for the scalar linear advection equation and its properties are analysed. Extensions of the CABARET scheme for quasi-linear scalar hyperbolic laws are presented in Section 3.1. In Section 3.2 the CABARET extensions to the Euler equations are provided. Numerical examples are assembled in Section 4.

2. CABARET scheme for linear advection

2.1. Single-time-step and -space-step scheme

A scalar conservation law

$$\partial_t u + \partial_x f(u) = 0 \tag{1}$$

is considered on a finite-difference grid which is non-uniform in space $x_{i+1} - x_i = h_{i+1/2}$ and time $t^{n+1} - t^n = \tau^{n+1/2}$. Fig. 1 shows the associated data structure on the non-uniform grid in space and time: the solid circles (labelled with letters) show the location of conservation variable u and the open circles (labelled with numbers) show the locations of flux variable f. Note that, contrary to a frequently used convention, the cells are labelled with fractional i-indices and the faces are labelled with whole i-indices. Our scheme assumes that all variables are known at the nth time level, and, then, it takes a half time step using forward-time central approximation, i.e., predictor step

$$\frac{u_C - u_E}{\frac{1}{2}\tau^{n+1/2}} + \frac{f_4 - f_5}{h_{i+1/2}} = 0. \tag{2}$$

It is continued with another half time step by using the backward-time central-space approximation, corrector step

$$\frac{u_A - u_C}{\frac{1}{2}\tau^{n+1/2}} + \frac{f_1 - f_2}{h_{i+1/2}} = 0, \tag{3}$$

where the fluxes f_1, f_2 are still to be determined. Note that by adding these two equations, one obtains a conventional flux integral around the cell 1–2–5–4, with a trapezoidal rule evaluation of the fluxes. By symmetry, the scheme will be second-order accurate for a sufficiently accurate evaluation of f_1 and f_2. We choose to evaluate these by a simple upwind extrapolation carried out in an upwind manner. Let's assume for the moment that the sign of the wave speed, $\partial_u f(u)$, is constant everywhere. Then, we determine $f_1 = f(u_1)$ by assuming that

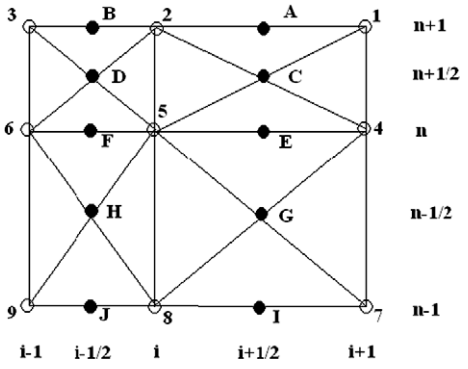

Fig. 1. Assumed data structure for the CABARET scheme for one dimension in space plus time. Solid circles denote conservation variables, open circles denote flux variables.

$$u_1 = 2u_C - u_5. \tag{4}$$

With this choice, the entire scheme (2)–(4) is time-reversible. It is also second-order accurate, regardless of the gird non-uniformity in space and time, and it is non-dissipative.

The predictor–corrector stages of the CABARER algorithm, (2) and (3) can be rearranged to an equivalent "delta" form, useful for solution convergence to a steady state [17]. This form does not use the conservation variables at the whole time levels:

$$u_C - u_G + \frac{1}{2}(\tau^{n+1/2} + \tau^{n-1/2})\frac{f_4 - f_5}{h_{i+1/2}} = 0, \tag{5}$$

where the flux variables are computed by the second-order extrapolation (4) that does not explicitly depend on the time step.

The algorithm (2)–(4), called CABARET [7,8] is an explicit single-step method. The scheme is conservative and stable under the Courant (CFL) condition: $0 \leqslant |c|\tau/h \leqslant 1$. Due to its extremely compact computational stencil CABARET retains its second-order approximation for non-uniform spatial and temporal grids.

Schemes similar to (2)–(4) exist in the literature; they are the Upwind Leapfrog (UL) schemes first discussed by Iserlis for linear advection [14], and later developed by Roe [26], Tran and Scheurer [34], and Kim [18] for multidimensional wave propagation. However these schemes were neither conservative with non-uniform grids, nor based on a compact one-space-cell one-time-step computational stencil. To see that the CABARET method reduces to the UL for the linear advection ($f = c \cdot u, c = const$) on a uniform grid in space and time, note that

$$u_C - u_E = v(u_5 - u_4) \quad \text{and} \quad u_E - u_G = v(u_5 - u_4), \tag{6}$$

where $v = c\tau/h$ is the CFL number. Hence,

$$u_C - u_E = v(u_5 - u_4) = \frac{1}{2}(u_1 + u_5 - u_4 - u_8) = \frac{1}{2}((u_1 - u_4) + (u_5 - u_8)), \tag{7}$$

which is the three-time-level UL method. In comparison to the CABARET stencil (1–A–2–C–4–E–5) the UL method (1–4–5–8) uses a double-interval computational stencil in time. In turn, in comparison to the conventional Central Leapfrog (Cross) method

$$v(u_6 - u_4) = (u_2 - u_8), \tag{8}$$

the UL scheme's stencil in space is twice smaller.

An important distinction between the implementations of the CABARET and UL schemes is that the UL scheme is three-time-level and needs to be properly initialized, otherwise a spurious mode can be excited. CABARET provides unambiguous prediction at level $(n + 1)$ from data at level (n). However, the same spurious mode can be excited if at the initial time step the flux data are not consistent with the conservation variables. For consistent initialisation, the fluxes at the initial time step can be determined by interpolation of conservation variables, or, more generally, by solving the corresponding Riemann problem.

In addition to removing the defects of the UL, the CABARET scheme retains all of the UL good properties, such as ease of implementation near boundaries, zero numerical dissipation and very small dispersion error.

2.2. Details of linear wave analysis

The non-staggered (UL) form of the CABARET scheme is well suited for analyzing its linear wave dissipation and dispersion properties. A travelling wave solution $\varphi_m^n \sim \exp[i\omega \cdot \tau \cdot n - ik \cdot h \cdot m]$ is substituted in (7) and the resulting algebraic equation is solved for the frequency, $\omega = \omega(k \cdot h)$, or $\frac{\omega \cdot \tau}{c \cdot k \cdot h} = f(k \cdot h, \mathrm{CFL})$, where f is a function of the dimensionless wave number, $k \cdot h$ and Courant number, $\mathrm{CFL} = |c|\tau/h$, to determine the dissipation $\Im m(\omega(k \cdot h) \cdot \tau) \neq 0$ and dispersion $f - 1 \neq 0$ errors as a function of wave and Courant numbers. The analysis shows that the CABARET scheme is non-dissipative $\Im m(\omega(k \cdot h) \cdot \tau) = 0$ for all wavenumbers $-\pi < k \cdot h < \pi$ and exact, $f = 1$ at three Courant numbers CFL = 0, 0.5 and 1.

Fig. 2 shows numerical surface of wave frequency normalised by dimensionless wavenumber, $f \sim 1$ for the CABARET scheme (a) and two standard second-order schemes, Central Leapfrog (Cross) (b), and Lax–Wendroff (LW) (c). Details of the CABARET dispersion surface for different Courant numbers are shown in Panels (d), (e) and (f). Apart from the two peaks of abnormal dispersion, which correspond to high wave and small CFL numbers (e.g. CFL < 0.1) (Fig. 2(d)), the CABARET dispersion surface does not show more than 5–10% deviation from the correct dispersion relation at wavenumbers $-\pi/2 < k \cdot h < \pi/2$. In comparison with CABARET in the same range of CFL and wavenumbers, the dispersion error of the conventional second-order central schemes (Fig. 2(b) and (c)) are larger by an order of magnitude. This is except the LW scheme at high CFL numbers, e.g. CFL > 0.8, which also correspond to a small dispersion error. However, note that in comparison with CABARET, the LW method is dissipative.

The problem of spurious dispersion peaks of the CABARET scheme at small CFL numbers can be rectified, without extending the scheme's stencil, by adding a linear space–time dissipative term into the original non-dissipative formulation (2)–(4). Indeed, consider replacing the extrapolation step (4) with

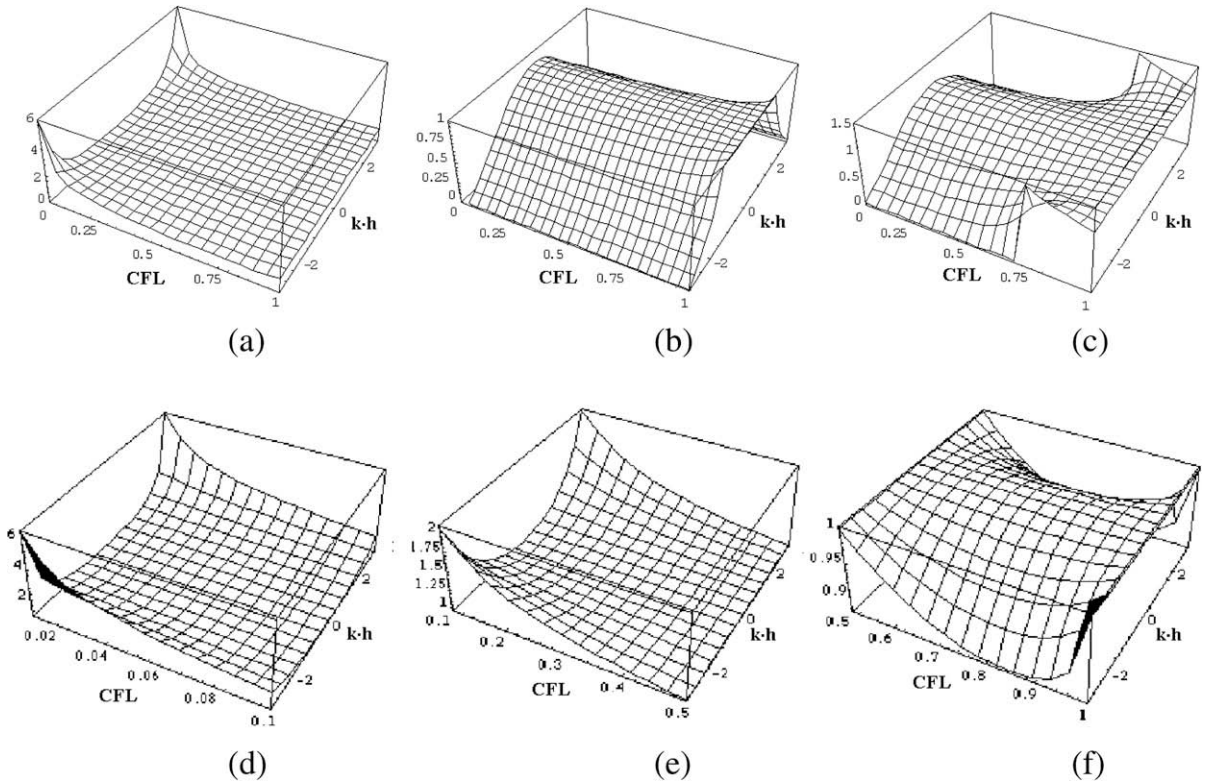

Fig. 2. Dispersion surfaces of (a) CABARET, (b) Cross, (c) Lax–Wendroff, and zoomed-in views of Panel (a) for (d) CFL < 0.1, (e) 0.1 < CFL < 0.5, and (f) 0.5 < CFL < 1.

$$u_1 = \frac{2}{1+\varepsilon}u_C - \frac{1-\varepsilon}{1+\varepsilon}u_5, \tag{4a}$$

where $0 \leqslant \varepsilon \leqslant 1$, so that for $\varepsilon = 0$ the extrapolation (4a) reduces to (4) and for $\varepsilon = 1$ the scheme (2), (3) and (4a) is identical to the first-order upwind scheme. Note that the CABARET method with linear space–time dissipation, (2), (3) and (4a) is equivalent to the following modification of the UL scheme:

$$v(u_5 - u_4) = \frac{1}{2}((1+\varepsilon)(u_1 - u_4) + (1-\varepsilon)(u_5 - u_8)). \tag{7a}$$

For more accuracy, the dissipation parameter can be made a function of CFL number. In particular, the function $\varepsilon(v) = \delta(1-v)(\frac{1}{2}-v)^2$ allows to turn the dissipation off at the two CFL numbers for which the original CABARET scheme (2)–(4) is exact. Fig. 3 shows the dispersion and dissipation surfaces of the CABARET scheme's modification (4a) for two values of δ. The use of dissipation parameter $\delta = 0.5$ ($\varepsilon \approx \frac{1}{8}$ for small CFL numbers) allows to completely remove the spurious

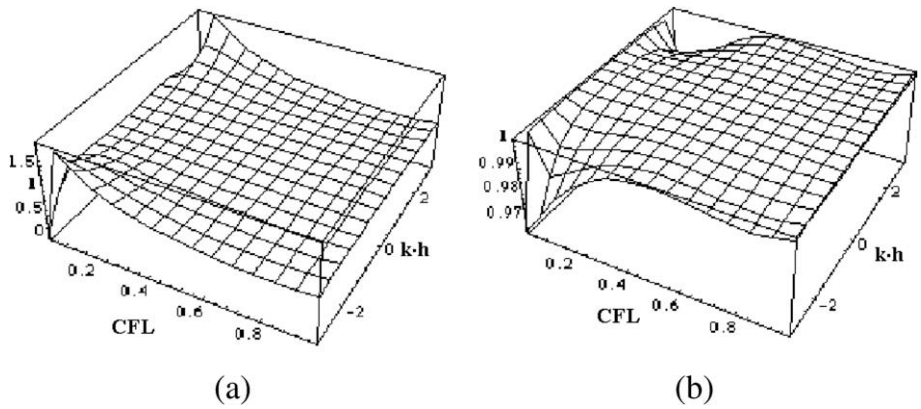

Fig. 3. Linear wave properties of the CABARET scheme with a linear dissipative term in space and time: (a) dispersion surface for $\delta = 0.5$, (b) dissipation surface for $\delta = 0.04$, notations are as in Fig. 2.

peaks of abnormal dispersion (a). Panel (b) shows that the dissipative effect of the CABARET modification (4a) is equivalent to a partial low-pass filtering at small CFL numbers.

As will be demonstrated in Section 4 and discussed in Appendix, the linear dissipative modification of CABARET (4a) can be useful for computing strongly non-linear problems with centred expansion waves. A more general approach for reducing the effect of dispersion error on the CABARET solution is discussed in Section 2.3.

To conclude this section, the dispersion properties of the CABARET scheme are compared against state-of-the-art low-dispersive semi-discrete finite-difference schemes. In the literature [5], it is common to compare the phase errors of finite-difference methods on a one-dimensional graph, $\varepsilon = \varepsilon(N_\lambda)$ where the number of grid points per wavelength, N_λ, is inversely proportional to the dimensionless wavenumber $N_\lambda = 2\pi/(k \cdot h)$. The phase error, which only considers the effect of spatial discretization, ε is defined as $\varepsilon = |K(k \cdot h) - k \cdot h|/\pi$, where the quantity $K(k \cdot h)$ represents the 'numerical' spatial wavenumber obtained by substituting the spatial part of the travelling wave solution $\exp[ik \cdot h \cdot m]$ into the spatial derivative $\frac{\partial \varphi}{\partial x}$.

Note that in comparison to the full space–time analysis in this case the influence of the temporal discretisation on dispersion error is ignored. Hence, the dispersion analysis of semi-discrete schemes correspond to exact integration in time. The comparison of these results with those of the fully discrete CABARET scheme is equivalent to comparing CABARET with semi-discrete spatial schemes used together with a temporal multi-stage Runge–Kutta (RK) scheme at an optimal CFL number that is small enough for RK to converge to the exact integration in time.

In Fig. 4 we compare the dispersion error of the fully-discrete CABARET scheme at different Courant numbers against the errors of semi-discrete finite differences including two state-of-the art high-order low-dispersion schemes used in turbulence modeling. Results for all central schemes are taken from [5]. We find that for most Courant numbers and for a wide range of grid resolution (7–20 points per wavelength) the dispersion error of the CABARET scheme remains below that of the conventional and optimised fourth-order central finite differences and close to that of the six-order central schemes. Away from the optimal Courant number range (CFL = 0.1), the CABARET dispersion error is similar to that of the fourth-order scheme.

For the range of grid resolutions considered in Fig. 4, the error decay rate (error slope) of the CABARET solution is between the forth- and the second-order schemes. For CABARET, the local error slope gradually reduces from 3.6 at $N_\lambda = 2$ to less than 3 for $N_\lambda > 100$. This suggests that for CABARET the error convergence rate in the norm of deviation from the exact dispersion relation is faster on coarse grids, when it is still converging to the theoretical value of 2.0.

Another important property pertaining to the numerical dispersion error is the numerical group speed (normalised by the advection speed), $c_g = \frac{\tau}{c}\frac{\partial(\omega(k\cdot h))}{\partial(k\cdot h)}$. Any deviation of c_g from 1 corresponds to an error in physical wave propagation. In particular, negative values of c_g lead to spurious wave reflection. In this case, all waves starting from a certain frequency are "grid locked" and their energy is back-scattered [5]. Fig. 5 shows the numerical group speeds of the same finite-difference schemes as in Fig. 4. It can be seen that all but the highest-order central schemes have $c_g < 0$ for waves shorter than 4 grid points per wavelength. In contrast, the CABARET group speed remains always positive, and the waves propagate at all frequencies. The magnitude of the CABARET c_g error is small: even for CFL = 0.1, it is similar to that of the fourth-order central differences in a wide range of wave numbers.

2.3. Non-linear correction method based on enforcing the maximum principle

The CABARET scheme (2)–(4) is second-order, and, according to the Godunov Theorem, it is not monotone, which, in turn, means it allows non-physical oscillations to emerge in the solution. For making the CABARET solution non-oscillatory, a simple tunable-parameter-free flux correction is introduced for the flux variables:

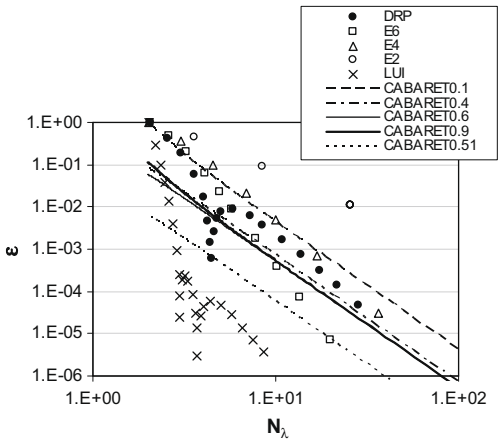

Fig. 4. Phase errors of several spatial finite-difference schemes and of the CABARET scheme at different CFL numbers *vs* grid resolution (number of grid points per wavelength, $N_\lambda = \pi/(k \cdot h)$). E2, E4, E6 denote standard central differences of the second, fourth and sixth-order, respectively, DRP denotes the fourth-order Dispersion Relation Preserving scheme [30]; and LUI stands for a sixth-order pentadiagonal compact scheme of Pade-type [20]. CABARET*x* stands for the CABARET scheme at Courant number CFL = *x*.

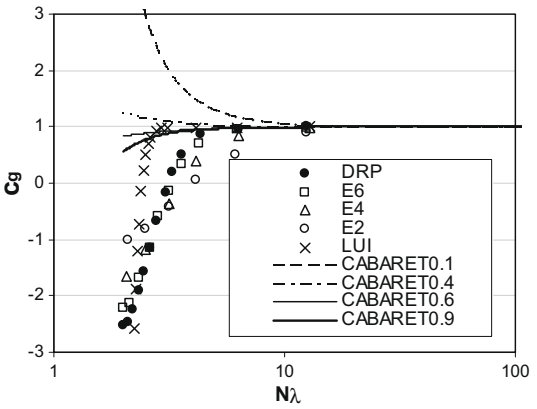

Fig. 5. Numerical group speeds of several central finite-difference schemes and of the CABARET scheme at different Courant numbers as functions of the grid resolution. The notations are the same as in Fig. 4.

$$
\begin{aligned}
&u_1 = 2u_C - u_5,\\
&\text{if } (u_1 > M)\ u_1 = M, \quad \text{if } (u_1 < m)\ u_1 = m,\\
&M = Max(u_4, u_E, u_5), \quad m = Min(u_4, u_E, u_5).
\end{aligned}
\tag{4b}
$$

The above non-linear correction procedure is based on the maximum principle for characteristic wave that arrives at point 1 from the solution domain dependency 4–E–5, and that is approximated using the 3-point stencil (u_4, u_E, u_5) within one cell in space. In comparison to the standard TVD schemes, the non-linear correction algorithm is directly based on enforcing the maximum principle on the solution rather than limiting the slopes of conservation variables. The CABARET flux correction (4b) does not explicitly enforce monotonicity on the conservation variables. Numerical tests, as well as the theoretical studies [23], have confirmed that the conservation variable solution of the CABARET method with flux correction (4a) remains strictly free from spurious oscillations for all Courant numbers CFL $\leqslant 0.5$. The extension of the fully non-oscillatory solution to higher CFL numbers, $0.5 < \mathrm{CFL} < 1$, is possible within the algorithm that in addition to the flux correction (4b) enforces the maximum principle on the conservation variable as well. For example, in the algorithm [9], after the conservation variables at mid-time-level are updated, e.g. in (2) or (5), the excess fields δ_C are calculated so that

$$
\begin{aligned}
&\delta_C = 0;\\
&if(u_C > Max(u_4, u_E, u_5)) \quad \delta_C = u_C - Max(u_4, u_E, u_5);\\
&if(u_C < Min(u_4, u_E, u_5)) \quad \delta_C = u_C - Min(u_4, u_E, u_5).
\end{aligned}
\tag{4c}
$$

The excess fields are then applied as the conservative correction fluxes to finally update the conservation variable

$$
\bar{u}_C = u_C - (\delta_C - \delta_B), \tag{4d}
$$

where the bar indicates the newly corrected conservation variable. A disadvantage of the above CABARET modification (4c) and (4d) is its increased complexity for non-linear problems and in the present work this type of algorithms will not be considered any further. Instead, here we will concentrate on simpler modifications of (4b).

Since the flux correction algorithm (4b) is based on approximating the maximum principle on a discrete 3-point stencil it leads to damping of the short wave solution components that are not well enough resolved on the stencil. While the selective damping introduced by flux limiting can be useful as a means for removing the under-resolved small scales from the solution in non-linear problems, e.g. [11], for high-frequency linear wave propagation this effect is undesirable. For CABARET, the dissipative effect of flux correction can be adjusted by making a slight change to the allowable monotonicity region. The corresponding single-parameter modification of the original flux correction algorithm (4b) is given below

$$
\begin{aligned}
&u_1 = 2u_C - u_5,\\
&if(u_1 > (1 + \alpha \cdot sign(M)) \cdot M) \quad u_1 = (1 + \alpha \cdot sign(M)) \cdot M,\\
&if(u_1 < (1 - \alpha \cdot sign(m)) \cdot m) \quad u_1 = (1 - \alpha \cdot sign(m)) \cdot m,\\
&M = Max(u_4, u_E, u_5), \quad m = Min(u_4, u_E, u_5),
\end{aligned}
\tag{4e}
$$

where $\alpha \geqslant 0$. The modified correction algorithm (4e) reduces to the basic flux correction algorithm (4b) for $\alpha = 0$ and to the non-dissipative CABARET scheme (4) for $\alpha \to \infty$. As it will be shown in Section 4, the range of empirical parameter variation is not large; its variation within $0 \leqslant \alpha \leqslant 0.01$ already yields very acceptable results.

3. Quasi-linear hyperbolic equations

3.1. Scalar conservation laws

For most CFD problems the sign of the wave speed is not constant, and there are two candidate choices to consider for each flux, e.g. $f_2 = f(u_2)$

$$(u_2)^+ = 2u_D - u_6 \quad \text{and} \quad (u_2)^- = 2u_C - u_4. \tag{9}$$

The values in (9) are corrected if found to be outside the allowable monotonicity region of the solution, similar to (4b). The bounds of the monotonicity region for each of the two candidate flux variables correspond to the domain dependency of characteristic waves that arrive at the flux face over 1 time step:

$$\begin{aligned} m^+ &= Min(u_5, u_E, u_6), \quad M^+ = Max(u_5, u_E, u_6); \\ m^- &= Min(u_4, u_F, u_5), \quad M^- = Max(u_4, u_F, u_5). \end{aligned} \tag{10}$$

For sign-constant wave speed, the choice in (9) is straightforward to make, e.g. for a positive speed the "plus" wave is selected.

For general case, the interface fluxes could be obtained from solving a Riemann problem between the 2 candidates, "plus" and "minus" flux states. However, in the present publication, a different approach for obtaining the solution is considered that is based on the characteristic decomposition. Examples of application of this approach are provided in Section 4. For the shock case, i.e., when the wavespeed in the upstream cell D is positive and the one in the downstream cell C is negative, the solution procedure is outlined below.

Let's first define the maximum and minimum solution values, $\varphi_{\min}$ and $\varphi_{\max}$, which correspond to the maximum and minimum flux, $f_2 = f(u_2)$ from the solution interval

$$\begin{aligned} &f(\varphi_{\min}) = f_m \quad \text{and} \quad f(\varphi_{\max}) = f_M, \\ &f_m = \min_{u_2 \in [(u_2)^+, (u_2)^-]} f(u_2) \quad \text{and} \quad f_M = \max_{u_2 \in [(u_2)^+, (u_2)^-]} f(u_2). \end{aligned} \tag{11}$$

Note that the maximum or minimum solution values do not correspond to the "plus" or "minus" flux values in case the maximum or minimum of the flux is between the two states, as it can be the case for a non-linear flux function (Section 4.2.3).

From the min and max values the cell-face variable is reconstructed according to the sign of the conservation variable variation at the mid time level

$$u_2 = \begin{cases} \varphi_{\max} & \text{if } u_C - u_D < 0, \\ \varphi_{\min} & \text{if } u_C - u_D \geqslant 0. \end{cases} \tag{12}$$

The updated value of the cell-face variable in (12) corresponds to the steepest local decay of the variation of conservation variable. Indeed, from (3) the conservation variable difference at the new time step is given by

$$u_A - u_B = u_C - u_D + \frac{1}{2}\tau^{n+1/2} f_2 \left(\frac{1}{h_{i+1/2}} + \frac{1}{h_{i-1/2}} \right) - \left[\frac{1}{2}\tau^{n+1/2} \left(\frac{f_1}{h_{i+1/2}} + \frac{f_3}{h_{i-1/2}} \right) \right], \tag{13}$$

and its variation is

$$\delta(u_A - u_B) = \delta(u_C - u_D) + \frac{1}{2}\tau^{n+1/2} \delta f_2 \left(\frac{1}{h_{i+1/2}} + \frac{1}{h_{i-1/2}} \right). \tag{14}$$

The algorithm of the flux reconstruction based on the minimal variation of conservation variable has similarity with the algorithm of reconstruction of Total Variation Bounded (TVB) solution used in ENO schemes. Indeed, in the latter, the choice between two possible candidate finite-difference stencils is given to the one which is smallest by magnitude.

Note that the same procedure of reconstructing flux variables from the conservation data (12) can be used at the initialisation step of the computation, where at the initial time step one may assume $(u_2)^+ = u_D$ and $(u_2)^- = u_C$.

3.2. Gas dynamics

Let's consider the one-dimensional Euler equations in conservative variables

$$\begin{aligned} &\frac{\partial \mathbf{U}}{\partial t} + \frac{\partial \mathbf{F}}{\partial x} = \mathbf{Q}, \\ &\mathbf{U}^{\mathrm{T}} = (\rho, \rho u, \rho E), \quad \mathbf{F}^{\mathrm{T}} = (\rho u, \rho u^2 + p, \rho u E + u p), \quad E = \varepsilon + u^2/2. \end{aligned} \tag{15}$$

In the above $\mathbf{F}$ is the flux vector of conservative variables $\mathbf{U}$; ρ is density; u is velocity; p is pressure; ε and E are internal and total energy; $Q = Q(\rho, \varepsilon, u, x, t)$ is the vector of source terms, which may include viscous forces, and the equation of state $p = p(\varepsilon, \rho)$ is assumed to satisfy

$$\frac{\partial p}{\partial \varepsilon}\cdot\frac{p}{\rho^2}+\frac{\partial p}{\partial \rho}=c^2 \geqslant \mu_0>0, \tag{16}$$

where c is the sound speed.

For cell $(i+1/2)$ the CABARET predictor–corrector steps (2) and (3) are

$$\frac{\mathbf{U}_C-\mathbf{U}_E}{\frac{1}{2}\tau^{n+1/2}}+\frac{\mathbf{F}_4-\mathbf{F}_5}{h_{i+1/2}}=\mathbf{Q}; \tag{17}$$

and

$$\frac{\mathbf{U}_A-\mathbf{U}_C}{\frac{1}{2}\tau^{n+1/2}}+\frac{\mathbf{F}_1-\mathbf{F}_2}{h_{i+1/2}}=\mathbf{Q}. \tag{18}$$

For the system of equations, the extrapolation step (4) requires the solution to be decomposed into characteristic fields [10].

Let's consider the characteristic form of the Euler equations

$$\frac{\mathbf{L}\cdot\partial\mathbf{V}}{\partial t}+\mathbf{\Lambda}\cdot\frac{\mathbf{L}\cdot\partial\mathbf{V}}{\partial x}=\widetilde{\mathbf{Q}} \tag{19}$$

where $\mathbf{L}$ and $\mathbf{\Lambda}$ are characteristic matrices, and $\mathbf{V}$ is the vector of primitive variables $(\rho,u,p)^T$. The characteristic form is directly obtained from (15) in the solution region away from the shocks.

In practice, there are very few cases when the increments of characteristic fields $d\mathbf{R}=\mathbf{L}\cdot d\mathbf{V}$ integrate to the full invariants, however, in the discrete representation the form of the local invariants may be important. Below several choices of local Riemann invariant definition are considered:

(i) Characteristic matrix is cell-wise constant

$$\mathbf{L}=\mathbf{L}_C=\begin{pmatrix}0 & 1 & (\rho_C\cdot c_C)^{-1}\\ 0 & 1 & -(\rho_C\cdot c_C)^{-1}\\ 1 & 0 & -(c_C)^{-2}\end{pmatrix}. \tag{20}$$

This leads to the vector of locally linearised Riemann invariants

$$\mathbf{R}^{\mathrm{T}}=(u+A\cdot p^{\mu},u-A\cdot p^{\mu},\rho-p(c_C)^{-2}),\quad A=(\rho_C\cdot c_C)^{-1},\quad \mu=1. \tag{21}$$

Under this choice all characteristic variables are linear functions of the primitive variables that is equivalent to the standard decomposition into simple characteristic waves, e.g. [13].

(ii) Pressure wave components of $\mathbf{L}$ are cell-wise constant, but the entropy wave components are variable in the cell

$$\mathbf{L}=\begin{pmatrix}0 & 1 & (\rho_C\cdot c_C)^{-1}\\ 0 & 1 & -(\rho_C\cdot c_C)^{-1}\\ -\gamma\rho^{-\gamma} & 0 & p^{-1}\end{pmatrix}, \tag{22}$$

which correspond to the following local Riemann invariants

$$\mathbf{R}^{\mathrm{T}}=(u+A\cdot p^{\mu},u-A\cdot p^{\mu},\ln(p\cdot\rho^{-\gamma})),\quad A=(\rho_C\cdot c_C)^{-1},\quad \mu=1. \tag{23}$$

Note that in comparison to (22) the third component of the local Riemann invariant in (23) is a non-linear entropy integral.

(iii) For the ideal gas equation of state, the characteristic matrix can be defined so that, at least in 1D case, the local Riemann invariants become full invariants for isentropic flows. Indeed, assuming cell-wise constant entropy

$$\mathbf{L}=\begin{pmatrix}0 & 1 & \frac{1}{\sqrt{\gamma}}(S_C)^{\frac{1}{2\gamma}}p^{-\frac{\gamma+1}{\gamma}}\\ 0 & 1 & -\frac{1}{\sqrt{\gamma}}(S_C)^{\frac{1}{2\gamma}}p^{-\frac{\gamma+1}{\gamma}}\\ -\gamma/\rho & 0 & 1/p\end{pmatrix},\quad S_C=p_C\cdot(\rho_C)^{-\gamma}, \tag{24}$$

yields

$$\mathbf{R}^{\mathrm{T}}=(u+Ap^{\mu},u-Ap^{\mu},\ln(p\cdot\rho^{-\gamma})),\quad A=\frac{2\sqrt{\gamma}}{\gamma-1}(S_c)^{\frac{1}{2\gamma}},\quad \mu=\frac{\gamma-1}{2\gamma}. \tag{25}$$

As will be discussed in Section 4, the use of the non-linear invariants (24) and (25) results in more accurate solution for several gas dynamics test cases.

In each case the transformation from the local Riemann invariants back to the primary variables is given by the following explicit relations:

$$u = \frac{1}{2}(R_1 + R_2), \quad p = \left(\frac{1}{2}(R_1 + R_2)/A\right)^{1/\mu}, \quad \rho = (\exp(R_3)/p)^{-1/\gamma}. \tag{26}$$

Once the solution field is decomposed into local invariants, the extrapolation step (4) is performed for each of the characteristic components, separately. In each cell, the "plus" and "minus" candidate flux variables are computed, according to the sign of their wave speed in the cell:

$$\begin{aligned} &(R_{q^+})_1 = 2(R_q)_C - (R_q)_5, \\ &(R_{q^-})_2 = 2(R_q)_C - (R_q)_4, \\ &q = 1,2,3. \end{aligned} \tag{27}$$

The local invariants are then subjected to the non-linear correction procedure:

$$m \leqslant (R_{q^+})_1 \leqslant M \quad \text{and} \quad m \leqslant (R_{q^-})_2 \leqslant M, \tag{28}$$

where the limits of the allowable monotonicity region are given by

$$\begin{aligned} &m = \min((R_q)_5, (R_q)_C, (R_q)_6) + \tau^{n+1/2} \cdot \widetilde{Q}_q, \\ &M = \max((R_q)_5, (R_q)_C, (R_q)_6) + \tau^{n+1/2} \cdot \widetilde{Q}_q, \quad q = 1,2,3, \end{aligned} \tag{29}$$

where $\widetilde{Q}_q$ are the sources in the 1D characteristic equations. Note that in comparison to (4b) the maximum and minimum values now include the source on right hand side of (19). The source term is calculated using the wave operator approximation to the second-order accuracy in space and first-order in time

$$\widetilde{Q}_q = \frac{(R_q)_C - (R_q)_C}{\tau^{n+1/2}/2} + (\lambda_q)_C \cdot \frac{(R_q)_4 - (R_q)_6}{h_{i+1/2}}. \tag{30}$$

At the end of the correction procedure there are 2 sets of local invariants computed for each cell face, e.g. $(R_{q^+})_2$ and $(R_{q^-})_2$. The selection procedure of a single flux vector from the 2 candidates, including the case when the face belongs to the boundary cell, is discussed in Appendix.

In the linearisation limit of the Euler equations, when the fluctuations of the flow quantities are small with respect to a constant mean flow, the CABARET scheme decouples into the system of scalar advection Eqs. (2), (3) and (4b) for each individual local Riemann invariant. For the non-linear local invariants (24) and (25), the CABARET algorithm based on the modified correction (4e) with a small $\alpha > 0$ leads to propagation of 1D acoustic waves without attenuation.

4. Numerical examples

4.1. Linear advection

The linear advection Eq. (1) with $c = 1$ is solved with the following initial conditions [1]

$$\begin{aligned} &\varphi(x_n(i), 0) = \sin\left(\frac{2\pi x_n(i)}{a \cdot h}\right) \exp\left(-\ln(2)\left(\frac{x_n(i)}{b \cdot h}\right)^2\right), \quad (a,b) = (8,3), \\ &-L/2 < x < L/2, \quad L = 100, \quad h = 1 \end{aligned} \tag{31}$$

on a set of uniform grids $x_n(i) = x_n(i-1) + \frac{h}{2^n}$, $n = 0, 1, \ldots$ Following the literature the error is defined in the relative norm: $\varepsilon = \sqrt{\frac{\sum(\varphi - \varphi_{exact})^2}{\sum \varphi_{exact}^2}}$.

Four schemes are considered: second-order Central Leapfrog scheme (Cross), Dispersion Relation Preserving scheme of Tam and Webb [30], sixth-order Optimised Central scheme (OS6) of Bogey and Bailly [1], and the CABARET scheme with the non-linear correction (2), (3) and (4b) (CABARET), which parameters are summarized in Table 1.

Fig. 6 shows the comparison between the Cross and CABARET solutions at time $t = 100$ at two CFL numbers, 0.2 and 0.8.

Table 1
Schemes compared in the linear advection test.

Scheme	Cross	DRP	OS6	CABARET
Order of approximation	2	4	6	2
Number of points per stencil	3	7	13	3
Number of temporal stages	1	4	6	1

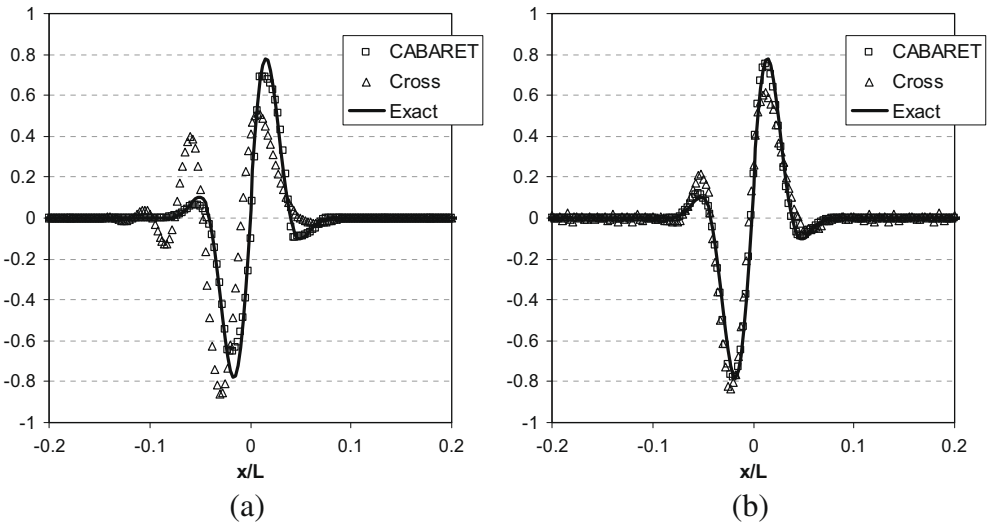

Fig. 6. Linear advection of the localised eddy profile at $t = 100$, (a) CFL = 0.2 and (b) CFL = 0.8.

It can be observed that the CABARET scheme leads to a more accurate solution in both calculations in comparison to Cross. The difference with the Cross scheme is particularly striking at CFL = 0.2 where the dispersion error of the Cross scheme is large, in accordance with the dispersion analysis results presented in Section 2.

Table 2 shows the error convergence results for all four central schemes against the CABARET scheme at $t = 800$. The solutions of the central schemes are shown for their optimal CFL numbers. Estimated CPU costs to reduce the numerical error down to about 5% for all three schemes are provided in Table 2a. The costs are calculated as a product of the grid resolution parameter, the number of points in the spatial stencil, and the number of temporal stages of each scheme.

It can be seen that the CABARET scheme remains more accurate for linear advection of the smooth initial distribution than the non-dissipative Cross scheme. As expected for a smooth solution, in comparison to the high-order finite-difference schemes optimised for linear advection the accuracy of the CABARET scheme on the same grid is less. Nevertheless, the CABARET scheme is considerably less CPU expensive per time step and its overall cost for the same solution accuracy is less for a wide range of Courant numbers. We find it remarkable since the high-order optimised finite-difference schemes are usually regarded as undisputed champions in efficiency for linear advection problems with smooth initial data, particularly over shock-capturing schemes [1].

In addition to the error in relative norm, the convergence of CABARET for several CFL numbers is checked in the standard L_2 norm $\varepsilon_2 = \sqrt{\frac{\sum(\varphi-\varphi_{exact})^2}{2^n}}$. The results in Table 3 show that the order of convergence for CFL < 0.5 is within 1.5–1.7 and for CFL > 0.5 it is close to 2. The same test run with CABARET, but without any flux correction, confirmed that its convergence rate in the same norm and on the same grids is, indeed, close to 2 for the entire CFL number range $0 < CFL < 1$. This suggests that the non-linear correction introduces produces a bigger effect on the solution for smaller CFL numbers, for which the dispersion error of CABARET is larger.

Table 2
Relative errors at $t = 800$.

	Cross	CABARET				7OS	13OS
CFL, n	0.9	0.4	0.5	0.6	0.9	0.2	0.8
0	1.98	0.878	0.410	1.39	1.43	1.30	**0.077**
1	1.46	0.575	0.208	1.13	1.15	0.713	
2	1.04	0.217	0.104	0.420	0.421	**0.082**	
3	0.308	0.095	0.052	0.130	0.129		
4	0.092	**0.034**	**0.026**	**0.044**	**0.045**		
5	**0.023**						

Table 2a
CPU cost (number of points per stencil × number of time stages × 2^n) for obtaining ~5% accuracy at $t = 800$.

Cross	CABARET	7OS	13OS
64	48	112	78

Table 3
L_2 convergence of the CABARET scheme with non-linear correction for the linear advection problem.

n	CFL = 0.2		CFL = 0.4		CFL = 0.6		CFL = 0.8	
	Error	Rate	Error	Rate	Error	Rate	Error	Rate
0	0.146		0.134		0.205		0.217	
1	0.134	0.124	0.092	0.54	0.156	0.382	0.188	0.204
2	0.090	0.576	0.038	1.29	0.050	1.64	0.074	1.35
3	0.037	1.30	0.016	1.21	0.0123	2.02	0.0185	2.00
4	0.016	1.19	0.005	1.53	0.003	2.03	0.0045	2.03
5	0.006	1.54	0.002	1.67	0.00075	2.02	0.001	2.02

4.2. Scalar conservation laws

4.2.1. Inviscid Burger's equation

The initial value problem for the scalar conservation law with the flux function $f(u) = u^2/2$ is considered next. The exact solution for the initial rectangular pulse distribution consists of a forerunning shock wave initiating from the right side of the pulse and a linear expansion wave, which tails off from the left.

Fig. 7 shows a computed cell-face-based solution at typical time moments for the Courant number, CFL = 0.25. The number of grid points is 100. The shock is well-resolved within 1–2 computational cells and both edges of the linear expansion wave are well captured. The analytical solution to this test problem is indistinguishable from the numerical curve. This is because the CABARET scheme is shock-capturing and the linear expansion wave is approximated exactly by the second-order extrapolation (4).

4.2.2. Buckley–Leverett equation

The Buckley–Leverett flux function $f(u) = \frac{u^2}{4u^2+(1-u)^2}$ is considered for the same initial rectangular pulse initial data and on the same grid. The solution behaviour is now more complex: there is an inflection point inside the solution interval $0 < u_0 < 1$, $\frac{d^2}{dx^2} f(u_0) = 0$, which leads to the solution structure that includes both shock and expansion wave for each, upstream and downstream, side of the pulse. For this problem, the strengths of the upstream and downstream shocks are known to be about 0.44 and 0.84, respectively (e.g. [15]).

Fig. 8 shows the numerical solution of the Buckley–Leverett problem corresponding to the initial and several consecutive time moments at Courant number CFL = 0.45. It can be seen that the fronts of the upstream and downstream shocks are well resolved, their strengths are accurately predicted, and the edges between the expansion waves and the solution plateau in the middle of the profile are sharply captured.

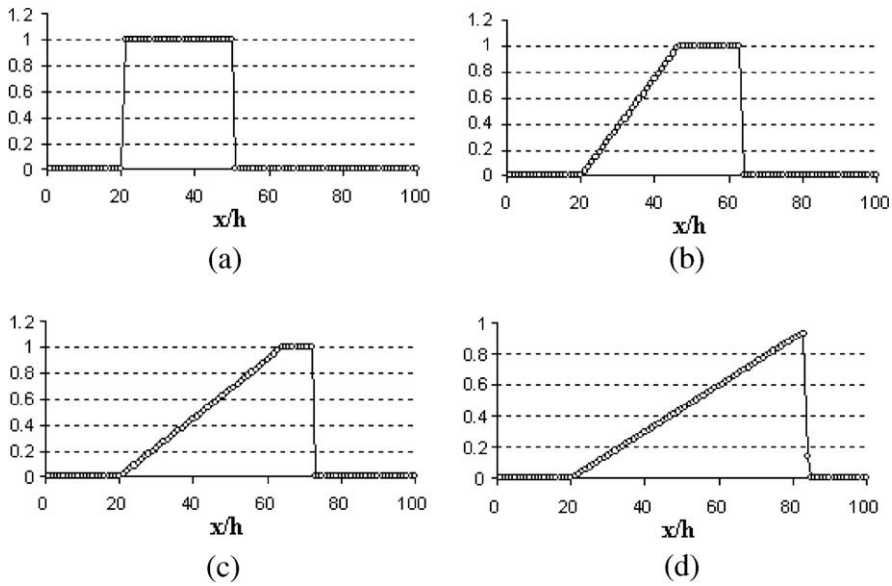

Fig. 7. Numerical solution to the inviscid Burgers problem at different time steps, (a) initial condition, (b) 60 time steps, (c) 100 time steps and (d) 150 time steps.

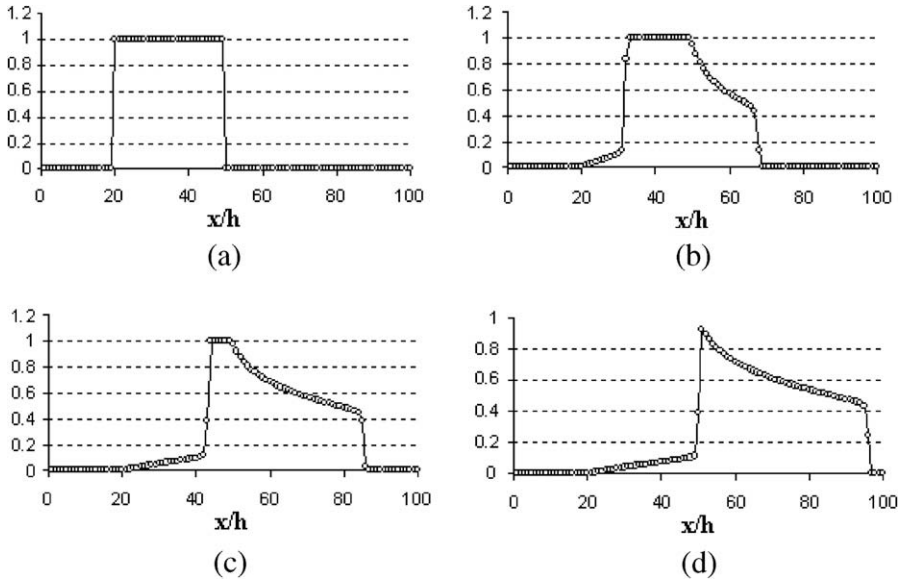

Fig. 8. Numerical solution to the inviscid Buckley–Leverett problem: (a) initial condition, (b) 50 time steps, (c) 100 time steps and (d) 130 time steps.

4.2.3. Smooth flux function with sonic points

The initial value problem for the flux function $f(u) = \sin(u)$ is considered for the following initial data

$$u(x,0) = \begin{cases} 0 & \text{if } x \leqslant 0, \\ \beta \cdot \pi & \text{if } 0 < x \leqslant 1, \\ 0 & \text{if } x > 1. \end{cases} \tag{32}$$

For $\beta > 1$ the flux function of the solution has inflection points. Several cases corresponding to different values of β are considered below.

- For $0 < \beta \leqslant 0.5$, the wave speed is always positive, and the cell-face variables, which correspond to the local minima and maxima of the flux function (11), are obtained from the minimum and maximum limit values of the two candidate solutions

$$\varphi_{\max} = \max((u^+)_2, (u^-)_2) \quad \text{and} \quad \varphi_{\min} = \min((u^+)_2, (u^-)_2). \tag{33}$$

- With including $0.5 < \beta \leqslant 1$ the first sonic point appears in the solution ($\beta = 0.5$). In this case the minimum and maximum limit values of the flux function (11) are approximated by

$$f_M = \max((f^+)_2, (f^-)_2, (f_S)_2) \quad \text{and} \quad f_m = \min((f^+)_2, (f^-)_2, (f_S)_2), \tag{34}$$

where $f^+ = f(u^+)$, $f^- = f(u^-)$ and $f_S = f(u_S)$ is such that $\left.\frac{df(u)}{du}\right|_{u=u_S} = 0$.

Note that in case of this non-linear flux function the additional value of flux (i.e., at the sonic point) is needed for obtaining a more accurate approximation of the non-linear flux function limits over the solution interval. The sonic point corresponds to $u_S = \pi/2$ and to calculate the solution values that correspond to (35) the following procedure is used

$$\begin{aligned} &\text{if } f_m = f_+, \quad \varphi_{\min} = (u^+)_2; \quad \text{if } f_M = f_+, \quad \varphi_{\max} = (u^+)_2; \\ &\text{if } f_m = f_-, \quad \varphi_{\min} = (u^-)_2; \quad \text{if } f_M = f_-, \quad \varphi_{\max} = (u^-)_2; \\ &\text{if } f_m = f_s, \quad \varphi_{\min} = (u_s)_2; \quad \text{if } f_M = f_s, \quad \varphi_{\max} = (u_s)_2. \end{aligned} \tag{35}$$

Fig. 9 shows the numerical solution for $\beta = 0.5$ and $\beta = 1$ at typical time moments. The number of grid points in the computational domain is 100. It can be noted that the shock waves and the edges of the expansion fan are well captured in both calculations.

For $1 < \beta \leqslant 2.5$, the wave speed changes its sign twice, and in order to take account for the additional inflection point, the Eq. (35) are supplemented by

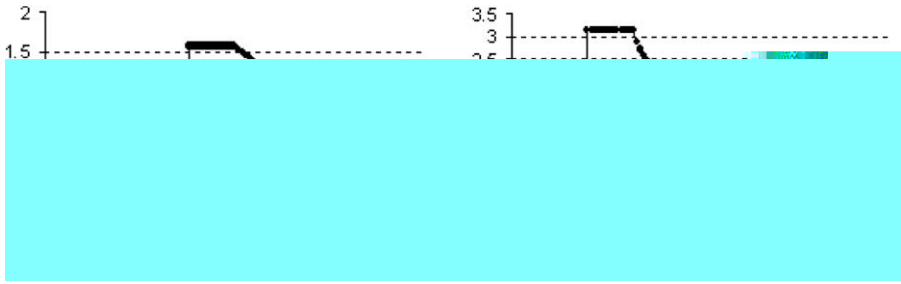

Fig. 9. Numerical solution to the sine flux function problem for (a) $\beta = 0.5$ at 60 time steps and (b) $\beta = 1$ at 40 time steps.

$$\begin{aligned} &\text{if } [M > \pi/2] \quad \text{and} \quad [m < \pi/2], \quad \varphi_{\max} = \pi/2; \\ &\text{if } [M > 3\pi/2] \quad \text{and} \quad [m < 3\pi/2], \quad \varphi_{\min} = 3\pi/2, \end{aligned} \tag{36}$$

where

$$M = \max((u^+)_2, (u^-)_2) \text{ and } m = \min((u^+)_2, (u^-)_2). \tag{37}$$

The solution method is extended to larger values of parameter β by taking into account newly emerging inflection points in a similar way. For example, in order to account for a new maximum of the flux function under $2.5 < \beta \leqslant 3.5$ the Eqs. (35)–(37) are supplemented by

$$\text{if } [M > 5\pi/2] \quad \text{and} \quad [m < 5\pi/2], \varphi_{\max} = 5\pi/2. \tag{38}$$

The numerical solutions for $\beta = 2$ and 3 at a typical time moment $NT = 40$ are shown in Fig. 10. It can be noted, again, that all shocks are well resolved within one cell and the edges of the expansion waves are crisply captured.

4.2.4. Non-smooth flux function with sonic points

A non-differentiable flux function $f(u) = |(u-1)^2 - 1|$ is considered for the following initial data

$$u(x,0) = \begin{cases} 0 & \text{if } x \leqslant 0; \\ 3 & \text{if } 0 < x \leqslant 1; \\ 0 & \text{if } x > 1. \end{cases} \tag{39}$$

In comparison with the previous case, the derivative of the flux function is discontinuous across the sonic points $u = 0$ and $u = 2$. However, for the algorithm based on the minimum variation of conservation variables, (11) and (12), the continuity of wave speeds is not important and the CABARET method remains equally robust and accurate. Fig. 11 shows solution snapshots at several typical time moments, the number of grid points is 100. As in the previous cases, all shock fronts and edges of the expansion waves are well captured.

4.3. Gas dynamics

4.3.1. Incoming acoustic wave test

The acoustic wave is specified as a sinusoidal pressure fluctuation of small amplitude about a constant mean flow:

$$\begin{aligned} &p^{(a)} = p_\infty + p', \quad p' = \varepsilon p_\infty \sin(2\pi x/\lambda - \omega t), \quad u^{(a)} = u_\infty + (p - p_\infty)/\rho_\infty c_\infty, \quad \rho^{(a)} = \rho_\infty \left(\frac{p}{p_\infty}\right)^{1/\gamma}; \\ &0 \leqslant x/L \leqslant 1, \quad \lambda/\Delta x = 14, \quad \omega = \frac{2\pi}{\lambda} c_\infty, \quad \varepsilon = 1.e-5, \quad \rho_\infty = 1, \quad u_\infty = 1, \quad p_\infty = 1. \end{aligned} \tag{40}$$

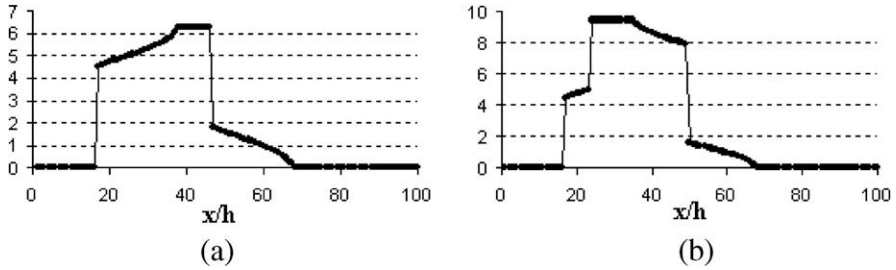

Fig. 10. Numerical solution to the sine flux function problem at 40 time steps, (a) $\beta = 2$ and (b) $\beta = 3$.

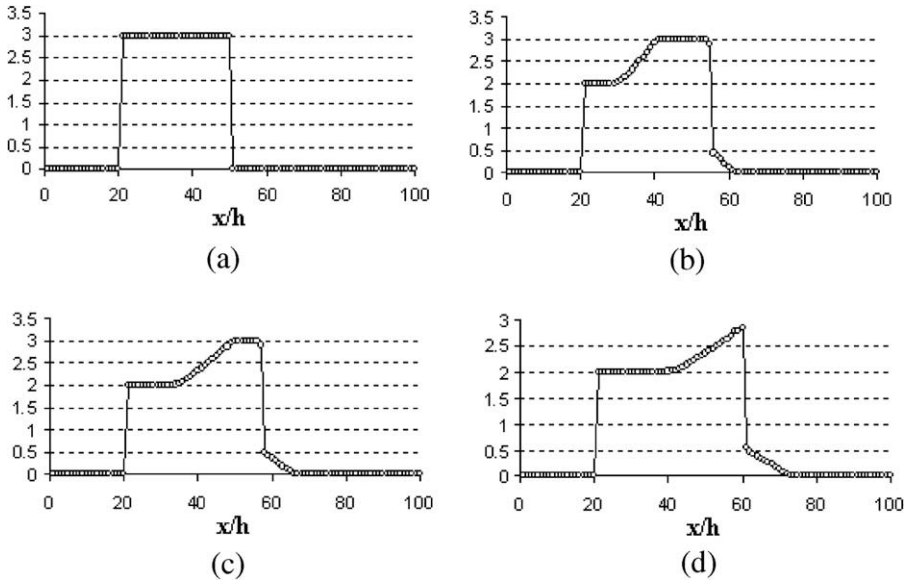

Fig. 11. Numerical solution to the non-smooth flux problem at different time steps, (a) initial condition, (b) 50 time steps, (c) 70 time steps and (d) 100 time steps.

The wave propagates into the computational domain from the subsonic inflow boundary specified at the left boundary $x = 0$. At the boundary the corresponding characteristic condition is used. In order to establish the sensitivity of the solution to the choice of local Riemann invariants the problem is solved with using different choices of Riemann variables discussed in Section 3.2.

Fig. 12(a) shows a typical solution snapshot of the local Riemann invariants, which are not consistent with entropy conservation for acoustic waves, (20) and (21). In these calculations, the local Riemann invariant that should propagate from the left boundary in fact also contains some pressure wave contribution going in the opposite direction. This leads to a spurious shift in phase and amplitude of the numerical solution (CABARET_L) in comparison with the exact solution. The same spurious effect also occurs for the non-linear Riemann invariants (21) and (22). In contrast to these, for the non-linear isentropic invariants (24) and (25) the numerical prediction (CABARET) almost coincides with the analytical solution (Fig. 12(b)).

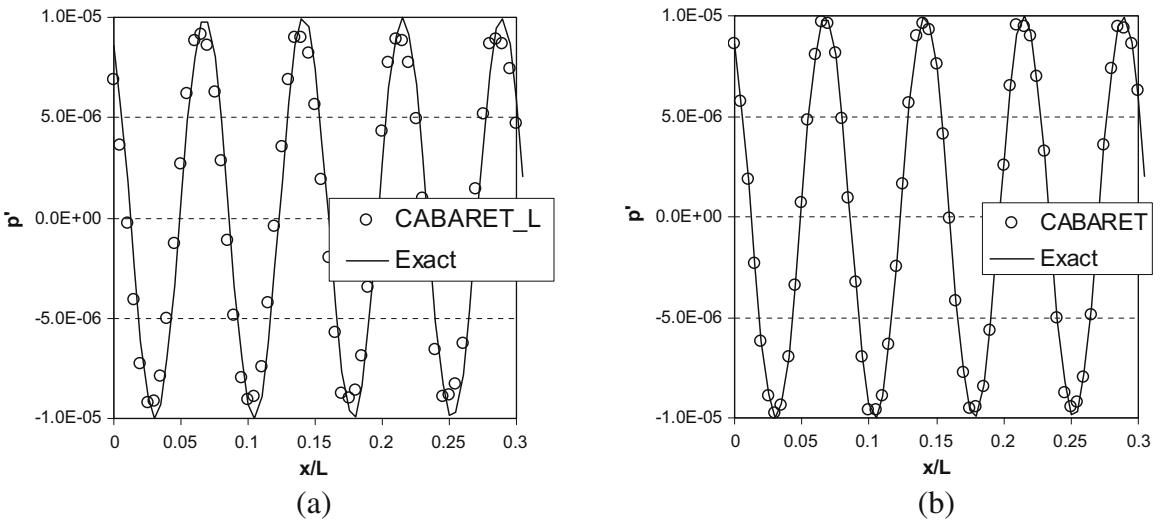

Fig. 12. Snapshot of computed acoustic pressure fluctuation *vs* the analytical solution: (a) solution based on locally linearised Riemann invariants (CABARE_L) and (b) solution based on the local Riemann invariants consistent for isentropic flows (CABARET).

4.3.2. Acoustic wave propagation on a non-uniform grid

The initial and boundary conditions of the problem correspond to a monochromatic acoustic wave propagating in zero mean flow field (Helmholtz problem) $p' = p(x,t) - \bar{p},\ p'/\bar{p} = \varepsilon \sin(\omega t - kx),\ k = \omega/\bar{c}$, where $\bar{p}$ and $\bar{c}$ are constant mean flow pressure and sound speed, and $\varepsilon = 10^{-5}$.

The full system of Euler equations is solved on a uniform grid with a sudden increase of the grid spacing at the centre of the computational domain

$$x_{i+1} - x_i = h \text{ for } 0 \leqslant x < 0.5 \quad \text{and} \quad x_{i+1} - x_i = m \cdot h \text{ for } 0.5 < x \leqslant 1. \tag{41}$$

The wave frequency is chosen so that the number of grid points per wavelength (ppw) $N_\lambda = 2\pi/(k \cdot h)$ in the left part of the domain is fixed and equal to 20. The problem is solved on a set of computational grids with the stretching parameter varying from $m = 1$ to $m = 3$. The maximum stretching parameter corresponds to the grid resolution of $N_\lambda = 6$–7.

Fig. 13 shows the comparison of the CABARET solutions with (a) and without (b) the non-linear correction procedure. The CABARET solution with the modified correction (4e) at $\alpha = 0.001$ leads to the same result as shown in Panel (b).

For all CABARET solutions, there is no spurious wave reflected from the coarse grid visible, which confirms that the method accuracy is not very sensitive to the grid singularity. It is observed that the use of the non-linear correction procedure leads to a linear attenuation of the under-resolved high-frequency solution with distance. Either without the correction or with the "relaxed" correction condition, the amplitude of the high-frequency solution remains well preserved.

4.3.3. Acoustic wave impinging on a contact discontinuity

The same Helmholtz wave propagation problem is considered, but this time on a uniform grid and with a contact discontinuity placed in the centre of the computational domain: $(\bar{\rho}_1, \bar{u}, \bar{p}) = (1, 0, 1)$ for $x < x_0$; $(\bar{\rho}_2, \bar{u}, \bar{p}) = (\beta, 0, 1)$ for $x > x_0$, for two cases $\beta = 0.1, 10$.

Upstream of the contact discontinuity the solution to this problem consists of the original impinging wave plus the reflected wave. Downstream of the discontinuity the solution is a single refracted wave. For linearised equations, the analytical solution is readily obtainable from the jump conditions across the discontinuity:

$$\begin{aligned} &p'(x,t)/\bar{p} = \varepsilon \sin(\omega t - k_1(x - x_0)) - \varepsilon \frac{1-\xi}{1+\xi} \sin(\omega t + k_1(x - x_0)) \quad \text{for } 0 \leqslant x \leqslant x_0, \\ &p'(x,t)/\bar{p} = \varepsilon \frac{2\xi}{1+\xi} \sin(\omega t - k_2(x - x_0)) \quad \text{for } x_0 < x < 0.5, \\ &\xi = \sqrt{\beta}, k_1 = \omega/\bar{c}_1, k_2 = \omega/\bar{c}_2, x_0 = 0.1 \quad \text{and} \quad \varepsilon = 10^{-5}, \end{aligned} \tag{42}$$

where $\bar{c}_1$ and $\bar{c}_2$ are sound speeds upstream and downstream of the discontinuity.

Fig. 14 shows the computed CABARET solutions against analytical for the dense-rarified case, $\beta = 0.1$ (a) and the rarified-dense case, $\beta = 10$. In both calculations the acoustic wave propagating in the dense medium corresponds to a coarse grid resolution of about 7 points per wavelength, and for this reason the modified correction procedure of the CABARET scheme (4e) is used with $\alpha = 0.001$. In both cases the agreement with the analytical solution is excellent and we note, again, that there is no sign of spurious reflection waves propagating from the location of the background field discontinuity.

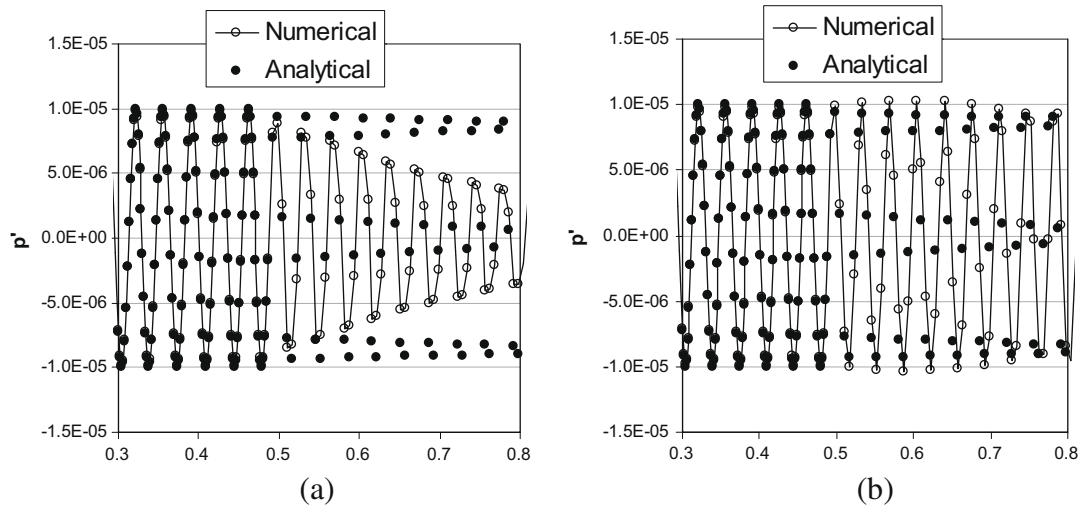

Fig. 13. Snapshot of computed acoustic pressure fluctuation *vs* the analytical solution at cell centres for the problem of linear acoustic wave propagation on a uniform flow field with a grid function discontinuity at $x = 0.5$ *vs* the analytical solution: (a) with the non-linear correction (4b) and (b) without the non-linear correction/with modified correction (4e) at $\alpha = 0.001$.

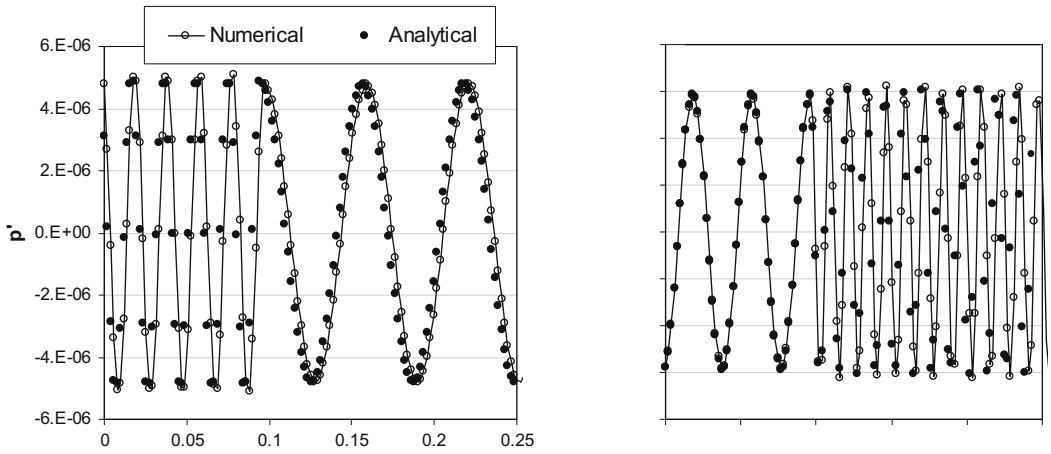

4.3.4. Propagation of a weak and strong shock wave

The propagation of a weak shock wave followed by a strong one is considered. The weak shock corresponds to the following conditions:

$$(\rho, u, p) = \begin{cases} (1.0000133, 0.0000157, 1.0000186) & \text{if } 0 < x/L < 0.1; \\ (1, 0, 1) & \text{if } 0.1 < x/L < 0.9, L = 1, \end{cases} \tag{43}$$

and the strong shock corresponds to

$$(\rho, u, p) = \begin{cases} (5.999964, 894.9159, 961051.5) & \text{if } 0 < x/L < 0.1; \\ (1.0000133, 0.0000157, 1.0000186) & \text{if } 0.1 < x/L < 0.9, L = 1. \end{cases} \tag{44}$$

This test presents a challenge for standard numerical schemes based on artificial viscosity since the numerical smoothing parameter needs to be separately adjusted for resolving the weak shock and for the computation stability in case of the strong shock. In comparison with these the computations performed with CABARET (27)–(29) are tuneable parameter free.

Fig. 15 shows computed density and pressure change with respect to the right state of the shock, $\rho' = \rho - \rho^{right}$ and $p' = p - p^{right}$ for the weak shock. The computational grid is 50 points. It can be seen that the shock front is captured within 3–4 cells. For the weak shock, the solution is found to be independent of the choice of the local Riemann invariants. Fig. 16

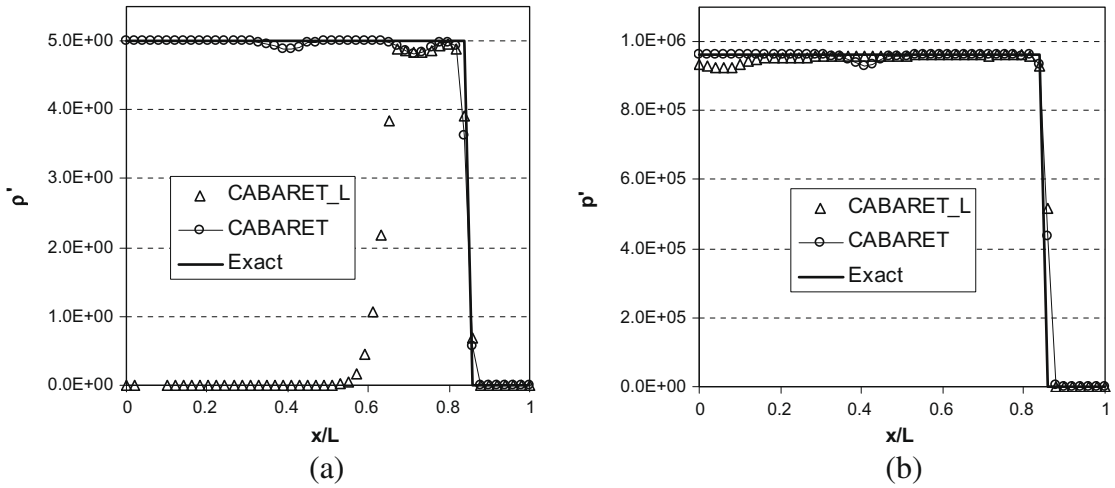

Fig. 16. Computed pressure solution corresponding of the strong shock problem: (a) density and (b) pressure.

shows results of the strong shock calculation for the same quantities as in Fig. 15. The solution (CABARET) obtained with the non-linear isentropic invariants (24) and (25) captures the shock front within 2–3 cells and has only a slight 'entropy trace' upstream of the shock that is not smeared by numerical viscosity. The CABARET algorithm based on the non-linear form (22) and (23) yields similar results. In contrast to these, the numerical solution for density based on the locally linearised invariants (CABARET_L) fails upstream of the shock front (Fig. 16(b)). This suggests that retaining at least some non-linear integral form of local invariants is important for the characteristic decomposition.

4.3.5. Strong supersonic shock-tube problem

Two supersonic shock-tube problems from [31] are considered next. The problems are modifications of the classical supersonic [29] shock-tube test with a higher density and pressure ratio between the initial gas states:

$$\text{Problem 1} : (\rho,u,p) = \begin{cases} (1000,0,1000) & \text{if } 0 \leqslant x/L < 0.3, \\ (1,0,1) & \text{if } 0.3 < x/L \leqslant 1, L = 1, \end{cases} \tag{45}$$

$$\text{Problem 2} : (\rho,u,p) = \begin{cases} (10000,0,10000) & \text{for } 0 \leqslant x < 0.3, \\ (1,0,1) & \text{for } 0.3 < x \leqslant 1, L = 1. \end{cases} \tag{46}$$

According to [31], the strong expansion waves generated downstream of the shock presents a challenge for popular non-oscillatory schemes for their velocity solution convergence in the vicinity of the shock front is very poor.

The displacement of the shock is not a local problem, but is due to smearing of the rarefaction wave, which, in turn, leads to mass being displaced from the correct shock position because of the conservation imposed. Therefore, this test not only

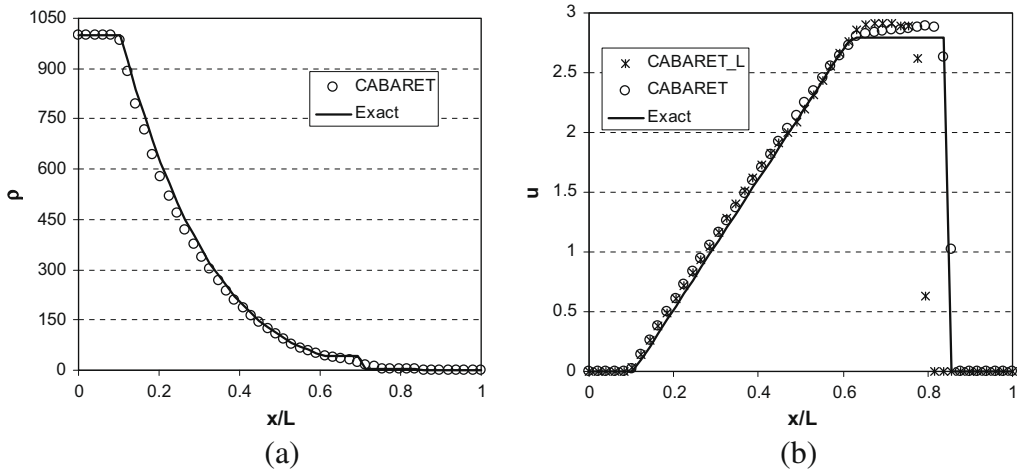

Fig. 17. Solutions of Problem 1 at a control time $t = 0.15$ of the CABARET scheme: (a) density and (b) velocity.

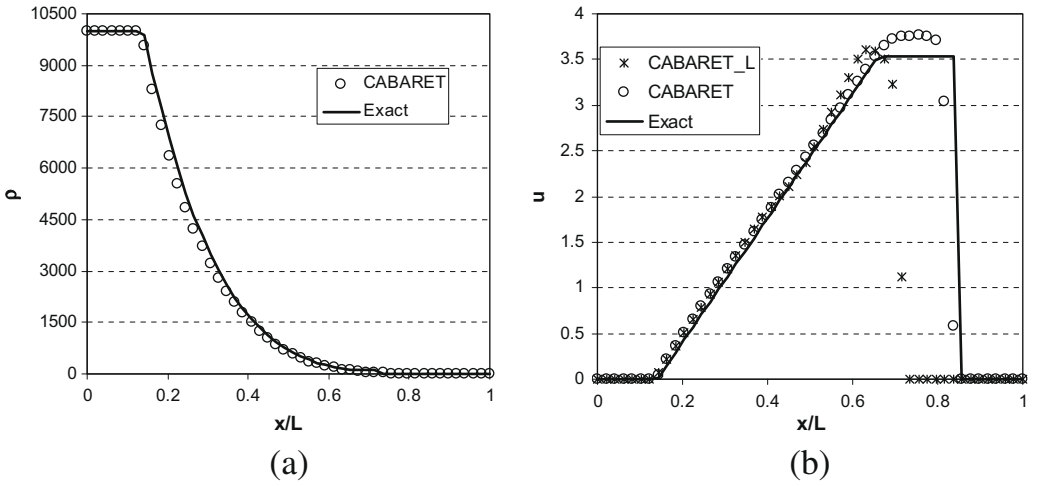

Fig. 18. Solutions of Problem 2 at a control time $t = 0.12$ of the CABARET scheme: (a) density and (b) velocity.

Table 4
Convergence of the CABARET scheme for Problem 2.

N	201	401	801	1601	3201	6401	12801	25601	51201
Log(L_1^h-error)	−1.025	−1.165	−1.397	−1.768	−2.349	−3.093	−3.234	−3.468	−3.727
Rate	0.464	0.770	1.233	1.929	2.471	0.467	0.776	0.862	

verifies the shock-capturing capability of the schemes but also how accurately they are able to resolve strong expansion fans with the shock displacement being a useful indicator of the combined effect.

Figs. 17 and 18 show the computed density and velocity profiles corresponding to problem 1 and 2 for the CABARET scheme with the locally linearised (20) and (21) (CABARET_L) and entropy-based (24) and (25) (CABARET) Riemann invariants. The computational grid is 50 points. The solutions for problem 1 correspond to control time $t = 0.15$ and the solutions for problem 2 correspond to $t = 0.12$.

It can be seen that in both cases the density solution obtained with the non-linear invariants (24) and (25) produces a notably lesser displacement of the shock in comparison with the locally linearised form. The density field is insensitive to the choice of local Riemann invariants for these test cases.

Table 4 shows the convergence results of the CABARET scheme in the standard L_1^h norm based on the velocity.

Fig. 19 compares the velocity zoomed in the vicinity of the shock computed with the CABARET scheme on two grids for problem 1 and 2 with the results obtained for the fifth-order WENO scheme [31]. As seen from the plots, the CABARET scheme results in a lesser shock displacement on the grids which are coarser by one order of magnitude.

4.3.6. Central expansion wave test

The next test case first considered in [33] corresponds to a strong central expansion wave which fronts move at a supersonic speed:

$$(\rho, u, p) = \begin{cases} (1, -2, 0.4) & \text{if } 0 \leqslant x/L < 0.5, \\ (1, 2, 0.4) & \text{if } 0.5 < x/L \leqslant 1, \quad L = 1. \end{cases} \tag{47}$$

This test is particularly difficult for low dissipative schemes because of the region of low internal energy emerging in the domain centre that leads to numerical instability. The CABARET algorithm with properly accounting for the singular sonic point, as discussed in Appendix, leads to a stable solution. Fig. 20 shows the computed velocity (a) and internal energy profile (b) for control time $t = 0.15$ by the CABARET scheme and the analytical solution. Panel (b) also shows the results for the modification of the first-order Roe flux-splitting scheme with the "entropy fix" from [27]. The number of grid points in both cases is 100. It can be seen that in comparison to the first-order scheme, the CABARET scheme leads to a lesser spurious peak of internal energy at the centre of expansion fan as well as to well-resolved edges of its fronts.

4.3.7. Blast wave problem

The blast wave problem [36] is considered next. At the initial time moment the computational box with reflective wall boundaries, $0 < x < 1$, is divided into three sections and each contains the same ideal gas at different initial conditions:

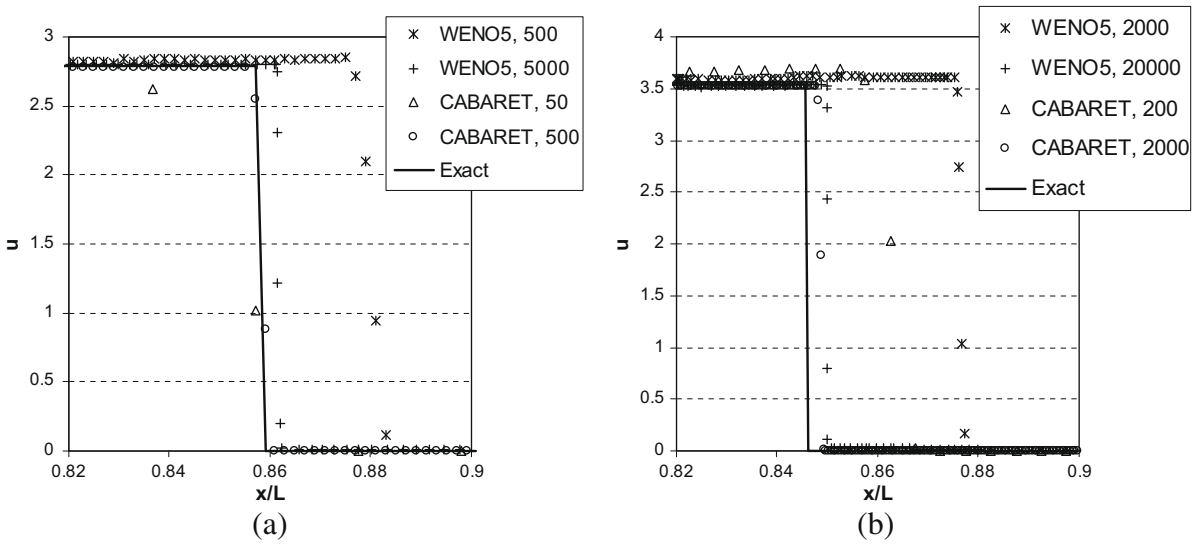

Fig. 19. A close-up view for the velocity profile across the shock: comparing the CABARET solution with the fifth-order WENO scheme (WENO5): (a) Problem 1, $t = 0.15$ and (b) Problem 2, $t = 0.12$.

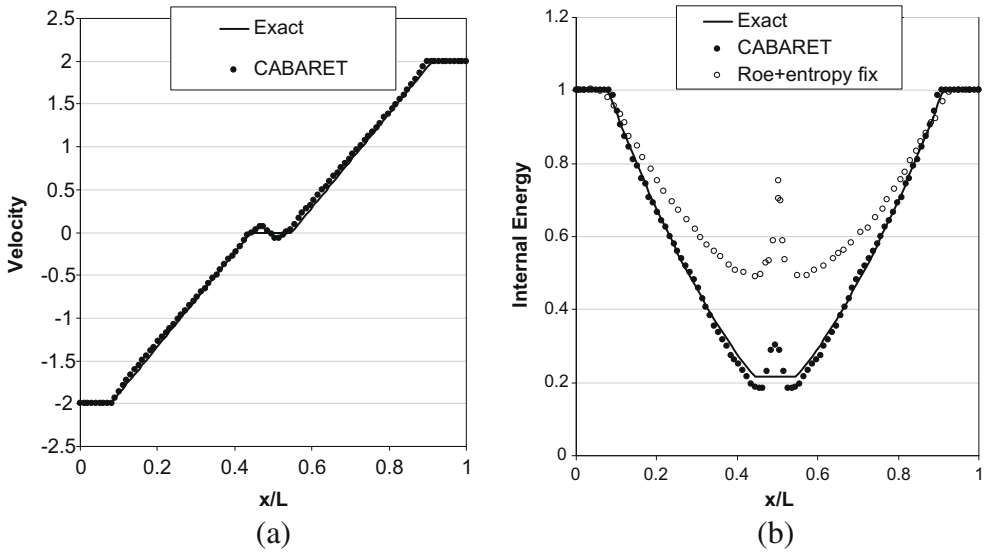

Fig. 20. Strong central expansion wave test (a) velocity and (b) internal energy at control time $t = 0.15$.

$$(\rho, u, p) = \begin{cases} (1, 0, 1000) & \text{if } 0 < x/L < 0.1; \\ (1, 0, 0.01) & \text{if } 0.1 < x/L < 0.9; \\ (1, 0, 100) & \text{if } 0.9 < x/L < 1, \quad L = 1. \end{cases} \tag{48}$$

The problem is solved on a set uniform grids with the number of cells, N, equal to 200, 300, 400, 600, 800, 1200, and 1600 and the results are compared with several popular shock-capturing schemes from the literature. The reference solution is obtained by computing the same problem at a fine grid $N = 4800$. All solutions correspond to control time $t = 0.038$. For this problem, all forms of the local Riemann invariants of the CABARET method lead to a similar solution.

Table 5 shows the computational errors defined in the standard L_1^h norm in density and the actual CPU costs for five different schemes. The notations used in the table for the methods other than CABARET are the same as in [36] and explained below:

- MC stands for an explicit second-order MacCormack scheme with an artificial viscosity;
- ETBFCT stands for a second-order the flux-correction algorithm [2];

4.3.8. Shock interaction with a density wave

The so-called Shu–Osher problem [28] is considered. A Mach number 3 shock impinges into a stationary density wave. The initial conditions, which correspond to exact conditions upstream of the shock and the density wave downstream, are prescribed as follows:

$$(\rho,u,p)=\begin{cases}(3.857143,2.629369,10.333333) \text{ for } x/L<0.1;\\ (1+\varepsilon\sin(k\cdot x),0,1) \text{ for } x/L\geqslant 0.1;\end{cases}$$
$$\varepsilon=0.2,\quad k=2\pi/\lambda,\quad \lambda/L=\frac{1}{8},\quad x\in[0,L]=10. \tag{49}$$

To compare with other numerical schemes, the problem is computed on five numerical grids N = 200, 400, 800, 1600, and 3200. For the CABARET scheme, the non-linear invariants (24) and (25) are used. The basic flux correction algorithm (4b), as well as the modified correction version (4e) are tested. The solutions with the tunable parameter-free CABARET version (4b) are considered first.

Following the literature, the numerical errors and total number of time iterations are summarized in Table 6. In the table, WENO is the third-order Weighted Essentially Non-Oscillatory Scheme and PLIMDE is the Parabolic Interpolation Method [4]. The total number of iterations corresponds to the number of time steps (NT) required to reach the control time moment, t = 1.8. To be consistent with the literature, the numerical error is evaluated in the following norms:

$$\varepsilon_1=\frac{1}{N+1}\sum\frac{|\rho-\rho_{exact}|}{|\rho_{exact}|};\quad \varepsilon_c=Max\left(\frac{|\rho-\rho_{exact}|}{|\rho_{exact}|}\right). \tag{50}$$

As follows from the table, the maximum error in the ε_c norm of the CABARET scheme is smallest among all three schemes, and its error in the ε_1 norm decays approximately linearly for all grid densities.

Fig. 22 shows a zoom of the CABARET solution on two grids N = 200 (a) and N = 400 (b) at the control time t = 1.8 against the reference converged solution that corresponds to N = 5000. The comparison with the reference solution on the 400-grid is very good, however, the 200-grid solution shows some smearing of the high-frequency oscillations upstream of the shock. To investigate the effect of the flux correction on the smearing of high-frequency structure, the same problem is calculated with the modified correction algorithm (4e) with α = 0.01. Fig. 23 shows that the results of the CABARET solution with the modified correction algorithm on the same grids computed at a slightly longer computational time t = 1.872. It can be seen that all post shock oscillations, except for the first upstream high-frequency ripple, are well resolved on the coarse grid.

Table 6
Relative errors for the shock/density wave interaction problem.

N	PLIMDE			WENO			**CABARET**		
	NT	ε_1	ε_c	NT	ε_1	ε_c	NT	ε_1	ε_c
200	250	0.0185	0.429	334	0.0214	0.902	**229**	**0.0219**	**0.1211**
400	468	0.0183	0.188	634	0.0195	0.667	**462**	**0.0100**	**0.1467**
800	903	0.0166	0.290	1235	0.0162	0.369	**927**	**0.0058**	**0.2400**
1600	1774	0.0070	0.185	2443	0.0040	0.572	**1856**	**0.0022**	**0.5338**
3200	3514	0.0024	0.230	4857	0.0013	0.399	**3716**	**0.0013**	**0.1324**

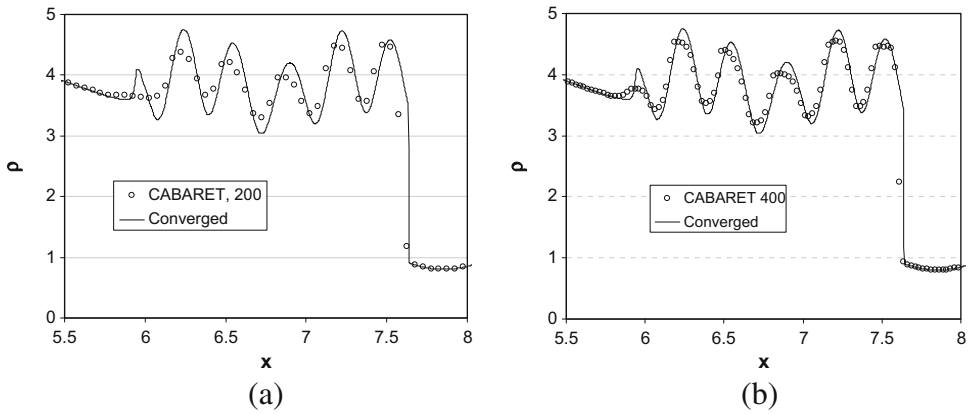

Fig. 23. Convergence of the CABARET with the modified flux correction (4e) for the shock/density wave interaction problem. Snapshots of density at control time t = 1.872. Notations are the same as in Fig. 22.

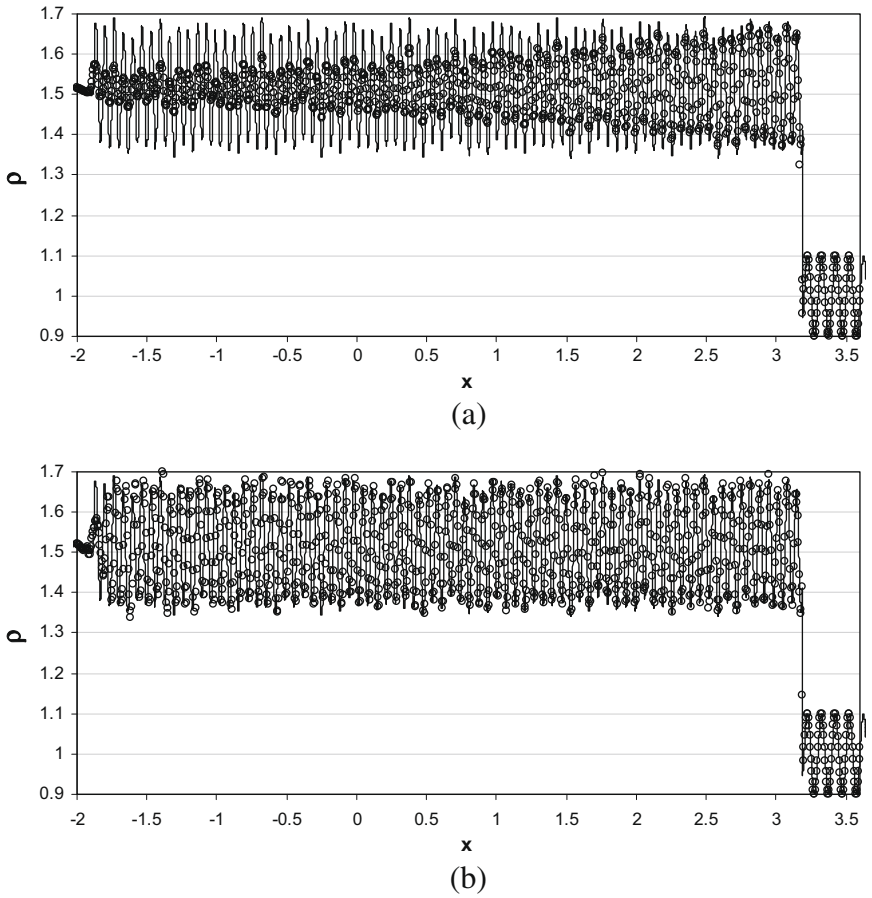

Fig. 24. Snapshot of the CABARET solution for the modified shock/density wave interaction problem at time $t = 5$ (a) with the basic flux correction algorithm and (b) with the modified flux correction algorithm.

Finally, to test the resolution capability of the CABARET algorithm with/without the flux correction modification the modified shock/turbulence interaction problem from [32] is considered. The initial conditions for this problem are given below

$$(\rho, u, p) = \begin{cases} (1.515695, 0.523346, 1.80500) & \text{for } x < -4.5, \\ (1 + 0.1\sin(20\pi x), 0, 1) & \text{for } x \geqslant -4.5, \end{cases} \tag{51}$$

which consists of a right-going shock wave of Mach number 1.1 impinging into a high-frequency density perturbation. The solution is computed for $t = 5$. In comparison to the original Shu–Osher test case both the solution time is much longer and the post shock oscillations are much finer in this test. Following the literature the grid is 2000 points and for the reference solution the grid of 20,000 points is used.

Fig. 24 shows the computed density profile in comparison with the reference solution for CABARET with and without the flux correction algorithm modification. The use of the basic flux correction (4b) leads to a gradual smearing of the high-frequency "saw" upstream of the shock. A similar solution smearing effect is observed for the fourth-order WENO-FORCE and WENO-FLIC schemes, as reported in [32]. The CABARET solution with the modified flux correction (4e) at $\alpha = 0.01$ does not show any attenuation of the high-frequency solution structure.

5. Conclusions and discussion

A new Compact Accurately Boundary-Adjusting high-REsolution Technique (CABARET) is presented for computational fluid dynamics problems. The new method has several clear distinctions in comparison with standard high-resolution methods in the literature.

- The fluxes of CABARET are calculated independently of the conservation variables. Unlike for standard finite-difference schemes, for the CABARET scheme the computation of fluxes does not involve any interpolation of conservation variables. Interpolation is always a well posed operation, hence, tends to be dissipative. In CABARET this is replaced by extrapolation which leads to low dissipation.

- CABARET is an explicit second-order scheme with very compact computational stencil in space and time that for linear advection is only one computational cell in space and time. The simplicity and compactness of the stencil lead to the ease of scheme implementation near the boundaries, with non-uniform grids and a low CPU cost per time iteration.
- The compact stencil is achieved by introducing auxiliary variables staggered in space and time. The introduction of auxiliary variables has been used in the literature before to increase the order of approximation without extending the stencil, e.g. in Discontinuous Galerkin methods. In comparison with these, in CABARET the auxiliary variables are introduced through upwind extrapolation. This leads to a fully discrete scheme in space and time that has non-dissipative and low-dispersive properties for linear wave propagation.
- For making solution non-oscillatory, CABARET uses a tuneable-parameter-free non-linear flux correction directly based on enforcing the maximum principle on flux variables, without explicitly modifying the conservation variables. This is different to the majority of FCT/TVD methods which use flux limiters that place bounds on the slopes of solution variation of the conservation variables.
- For CABARET, plentiful numerical tests have demonstrated that the non-linear flux correction based on the maximum principle leads to an accurate balance between the dispersion and dissipation errors. In this respect CABARET with non-linear flux correction can be regarded as a new successful upgrade of the first-order Godunov scheme to second-order. Indeed, in comparison with the latter CABARET does not only retain the original stencil compactness, low dispersion and boundness properties of the solution but also has a very small dissipation error.

It has been demonstrated that the basic tuneable-parameter-free flux correction algorithm used in CABARET can be modified to further increase the solution accuracy by using a single tuneable parameter. For a range of linear/non-linear problems, it has been shown that the small parameter variation within 0.001–0.01 allows to accurately capture the fine solution structure without smearing on coarse grids.

The extension of CABARET for systems of equations is based on the method of characteristic decomposition with using local Riemann invariants. Due to the independence of flux and conservation variables the local Riemann invariants can be introduced to emphasise additional properties of the flow equations without affecting the conservation. For example, it has been shown that for a range of gas dynamics test cases the non-linear form of local Riemann invariants that correspond to the full Riemann invariants for 1D isentropic flows leads to more robust and accurate results in comparison with the local invariants based on the cell-wise linearisation.

The results presented in the paper are concerned with CABARET for 1D fluid dynamics problems. Systematic description of CABARET extensions to multiple dimensions and higher-order approximation will be the subject of future publications.

Acknowledgments

The authors would like to acknowledge with gratitude the support of the Royal Society of London. The research was supported by the Russian Foundation for Basic Research (Grant Nos. 06-01-00293a and 06-01-00819a). Discussions with Philip Roe are graciously appreciated.

Appendix A. Reconstruction of the characteristic flux vector

A.1. General procedure

Let's define the signs of the characteristic speeds at the cell face 2 according to the interpolation rule

$$\begin{aligned} &sign(u+c) = sign((u+c)_C + (u+c)_D),\\ &sign(u-c) = sign((u-c)_C + (u-c)_D),\\ &sign(u) = sign(u_C + u_D) \end{aligned} \tag{A.1}$$

and use the "plus" or "minus" components of the characteristic vector that arrive in face 2 from cells C and D.

Then one of the following cases is possible:

- Subsonic flow to the right

$$sign(u+c) > 0, \quad sign(u-c) < 0, \quad sign(u) > 0, \tag{A.2}$$

which leads to the solution vector at the cell face

$$(\mathbf{R}_2)^{\mathrm{T}} = ((R_{1^+})_2, (R_{2_-})_2, (R_{3^+})_2); \tag{A.3}$$

- Subsonic flow to the left

$$sign(u+c) > 0, \quad sign(u-c) < 0, \quad sign(u) < 0, \tag{A.4}$$

which corresponds to

$$(\mathbf{R}_2)^{\mathrm{T}} = ((R_{1^+})_2, (R_{2_-})_2, (R_{3^-})_2); \tag{A.5}$$

- Supersonic flow to the right

$$sign(u+c) > 0, \quad sign(u-c) > 0, \quad sign(u) > 0, \tag{A.6}$$

and the corresponding solution vector is

$$(\mathbf{R}_2)^{\mathrm{T}} = ((R_{1^+})_2, (R_{2_+})_2, (R_{3^+})_2); \tag{A.7}$$

- Supersonic flow to the left

$$sign(u+c) < 0, \quad sign(u-c) < 0, \quad sign(u) < 0, \tag{A.8}$$

which corresponds to

$$(\mathbf{R}_2)^{\mathrm{T}} = ((R_{1^-})_2, (R_{2_-})_2, (R_{3^-})_2). \tag{A.9}$$

A.2. Special cases

The general procedure outlined in the previous section is modified for one of the special cases considered below.

The location of a sonic point $u \pm c = 0$ between the left and right cells requires a separate consideration. The following scenarios are possible:

(i) Subsonic flow to the right in the left cell and supersonic flow to the right in the right cell

$$(u+c)_D > 0, \quad (u-c)_D < 0, \quad u_D > 0 \quad \text{and} \quad (u+c)_C > 0, \quad (u-c)_C > 0, \quad u_C > 0; \tag{A.10}$$

(ii) Supersonic flow to the left in the left cell and subsonic flow to the left in the right cell

$$(u+c)_D < 0, \quad (u-c)_D < 0, \quad u_D < 0 \quad \text{and} \quad (u+c)_C > 0, \quad (u-c)_C < 0, \quad u_C < 0. \tag{A.11}$$

From the two characteristics coming to the cell face two equations are obtained. The missing condition needed to close the system of equations can be obtained from the second-order interpolation between the two cells

$$u_2 = \frac{1}{2}(M_D + M_C)c^*, \quad M_C = u_C/c_C \quad \text{and} \quad M_D = u_D/c_D, \tag{A.12}$$

where $c^* = B(p_2)^{\mu}$, $B = c_C \cdot (p_C)^{-\mu}$ and μ is the exponent in the definition of the local Riemann invariant.

The other special case which deserves a special treatment is the case of a centred expansion wave, which fronts move with supersonic speeds:

$$(u+c)_D < 0, \quad (u-c)_D < 0, \quad u_D < 0 \quad \text{and} \quad (u+c)_C > 0, \quad (u-c)_C > 0, \quad u_C > 0. \tag{A.13}$$

In this case a simple modification of the algorithm described in (A.1) is to introduce linear dissipation in the cell which contains the singular sonic point, i.e. instead of (27) use

$$\begin{aligned} (R_{q^+})_1 &= \frac{2}{1+\varepsilon}(R_q)_C - \frac{1-\varepsilon}{1+\varepsilon}(R_q)_5, \\ (R_{q^-})_2 &= \frac{2}{1+\varepsilon}(R_q)_C - \frac{1-\varepsilon}{1+\varepsilon}(R_q)_4, \quad q = 1,2,3, \end{aligned} \tag{A.14}$$

where $0.5 < \varepsilon < 1$. For example in test case 4.3.6 the value $\varepsilon = 0.7$ is used.

A standing alone case is when two characteristics $(R_{q^+})_2$ and $(R_{q^-})_2$ coming to the cell face correspond to the same eigenvalue λ_q and there is a choice which local Riemann invariant to use for the face flux. In this case the algorithm based on the principle of minimal variation of the conservation variable (Section 3.1) is applied

$$(R_q)_2 = \begin{cases} \varphi_{\max} & \text{if } (R_q)_C - (R_q)_D < 0, \\ \varphi_{\min} & \text{if } (R_q)_C - (R_q)_D \geqslant 0, \end{cases} \tag{A.15}$$

where

$$\begin{aligned} &f(\varphi_{\min}) = f_m \quad \text{and} \quad f(\varphi_{\max}) = f_M, \\ &f_m = \min[(\lambda_q)_D R_{q^+}, (\lambda_q)_C R_{q^-}] \quad \text{and} \quad f_M = \max[(\lambda_q)_D R_{q^+}, (\lambda_q)_C R_{q^-}]. \end{aligned} \tag{A.16}$$

Note that in comparison to the algorithm (11) and (12) applicable to general non-linear flux functions the flux functions in (A.16) are linear, hence, their maximum and minimum values are used.

A.3. Boundary conditions

There are five standard types of the boundary conditions for the 1D Euler equations: (i) supersonic inflow, (ii) subsonic inflow, (iii) supersonic outflow, (iv) subsonic outflow and (v) inviscid hard wall. Assuming that the external boundary lies between cells A and B with B being external to the flow, these are listed below:

(i) All cell-face values are specified according to the flow conditions at infinity

$$\rho_2 = \rho_\infty, \quad u_2 = u_\infty, \quad p_2 = p_\infty. \tag{A.17}$$

(ii) Two incoming local Riemann invariants are extrapolated from the infinity and one outgoing is calculated from the domain interior

$$(u_2 + A_D(p_2)^\mu, u_2 - A_C(p_2)^\mu, \ln(p_2 \cdot (\rho_2)^{-\gamma})) = ((R_1)_D, (R_2)_2, (R_3)_D). \tag{A.18}$$

(iii) All variables are calculated from the domain interior

$$(u_2 + A_C(p_2)^\mu, u_2 - A_C(p_2)^\mu, \ln(p_2 \cdot (\rho_2)^{-\gamma})) = ((R_1)_2, (R_2)_2, (R_3)_2). \tag{A.19}$$

(iv) One incoming invariant is extrapolated from the condition at infinity and the remaining local invariants are calculated from the interior

$$(u_2 + A_D(p_2)^\mu, u_i^{n+1} - A_C(p_2)^\mu, \ln(p_2 \cdot (\rho_2)^{-\gamma})) = ((R_1)_\infty, (R_2)_2, (R_3)_2). \tag{A.20}$$

(v) The incoming Riemann variable is obtained from the condition of satisfying zero velocity on the boundary and the entropy is updated according to the velocity sign in cell C:

$$\left(u_2 + A_C(p_2)^\mu, u_1^{n+1} - A_C(p_2)^\mu, \ln(p_2 \cdot (\rho_2)^{-\gamma})\right) = (-(R_2)_2, (R_2)_2, (R_3)_2), \quad \text{if } u_C \leqslant 0 \tag{A.21}$$

and

$$(u_2 + A_C(p_2)^\mu, u_1^{n+1} - A_C(p_2)^\mu, \rho_2) = (-(R_2)_2, (R_2)_2, \rho_C) \quad \text{if } u_C > 0. \tag{A.22}$$

References

[1] C. Bogey, C. Bailly, A family of low dispersive and low dissipative explicit schemes for flow and noise computations, J. Comput. Phys. 194 (2004) 194–214.
[2] J.P. Boris, D.L. Book, K. Hain, Flux-corrected transport: generalization of the method, J. Comput. Phys. 31 (1975) 335–350.
[3] B. Cockburn, C.-W. Shu, Runge–Kutta discontinuous Galerkin methods for convection-dominated problems, SIAM J. Sci. Comput. 16 (2001) 173–261.
[4] P. Colella, P.R. Woodward, The piecewise parabolic method (PPM) for gas-dynamical simulations, J. Comput. Phys. 54 (1984) 174–201.
[5] T. Colonius, S.K. Lele, Computational aeroacoustics: progress on nonlinear problems of sound generation, Prog. Aerospace Sci. 40 (2004) 345–416.
[6] S.K. Godunov, A difference scheme for numerical computation of discontinuous solutions of equations of fluid dynamics, Math. Sbornik 47 (1959) 271–306.
[7] V.M. Goloviznin, A.A. Samarskii, Difference approximation of convective transport with spatial splitting of time derivative, Math. Model. 10 (1998) 86–100.
[8] V.M. Goloviznin, A.A. Samarskii, Some properties of the CABARET scheme, Math. Model. 10 (1998) 101–116.
[9] V.M. Goloviznin, S.A. Karabasov, I.M. Kobrinski, Balanced-characteristic schemes with staggered conservative and transport variables, Math. Model. 15 (2003) 29–48.
[10] V.M. Goloviznin, Balanced characteristic method for systems of hyperbolic conservation laws, Doklady Math. 72 (2005) 619–623.
[11] F.F. Grinstein, L. G Margolin, W.J. Rider, Implicit Large Eddy Simulation: Computing Turbulent Dynamics, Cambridge University Press, New York, 2007.
[12] A. Harten, B. Engqist, S. Osher, S. Chakravarthy, Uniformly high order accurate essentially non-oscillatory schemes III, J. Comput. Phys. 71 (1987) 231–303.
[13] C. Hirsch, Numerical Computation of Internal and External Flows. The Fundamentals of Computational Fluid Dynamics, second ed., John Wiley & Sons, Ltd., Elsevier, 2007.
[14] A. Iserles, Generalized Leapfrog methods, IMA J. Numer. Anal. 6 (1986) 381–392.
[15] G.-S. Jiang, D. Levy, C.-T. Lin, S. Osher, E. Tadmor, High-resolution non-oscillatory central schemes with non-staggered grids for hyperbolic conservation laws, SIAM J. Numer. Anal. 35 (1998) 2147–2168.
[16] S.A. Karabasov, V.M. Goloviznin, New efficient high-resolution method for nonlinear problems in aeroacoustics, AIAA J. 45 (2007) 2861–2871.
[17] H.B. Keller, Computational Fluid Dynamics, AMS Bookstore, 1978.
[18] S. Kim, High-order upwind leapfrog methods for multidimensional acoustic equations, Int J. Numer. Mech. Fluids 44 (2004) 505–523.
[19] V.P. Kolgan, The application of a minimal solution slope principle for the development of finite-difference schemes for solving gas dynamics problems with discontinuities, Uch. Zapiski TsAGI 3 (1972) 68–77.
[20] S.K. Lele, Compact finite-difference scheme with spectral-like resolution, J. Comput. Phys. 103 (1992) 16–42.
[21] X.-D. Liu, S. Osher, T. Chan, Weighted essentially non-oscillatory schemes, J. Comput. Phys. 115 (1994) 200–212.
[22] S. Osher, S. Chakravarthy, High resolution schemes and the entropy condition, SIAM J. Numer. Anal. 21 (1984) 984–995.
[23] V.V. Ostapenko, On the monotonicity of the balanced-characteristic scheme, Math. Model. 21 (2009) 29–42.
[24] J. Qiu, C.-W. Shu, Runge–Kutta discontinuous Galerkin method using WENO limiters, SIAM J. Sci. Comput. 26 (2003) 907–929.
[25] P.J. Roache, Computational Fluid Dynamics, Hermosa, Albuquerque, 1982.
[26] P.L. Roe, Linear bicharacteristic schemes without dissipation, SIAM J. Sci. Comput. 19 (1998) 1405–1427.

[27] A.V. Safronov, A stabilization technique for characteristic finite-difference schemes for solving gas dynamics problems, Comput. Methods and Program. 8 (2007) 6–9.
[28] C.-W. Shu, S. Osher, Efficient implementation of essentially non-oscillatory shock-capturing schemes, J. Comput. Phys. 77 (1988) 439–471.
[29] G.A. Sod, A survey of several finite difference methods for systems of nonlinear hyperbolic conservation laws, J. Comput. Phys. 27 (1978) 1–31.
[30] C.K.W. Tam, J.C. Webb, Dispersion-relation-preserving finite difference schemes for computational acoustics, J. Comput. Phys. 107 (1993) 262–281.
[31] H. Tang, T. Liu, A note on the conservative schemes for the Euler equations, J. Comput. Phys. 218 (2006) 451–459.
[32] V.A. Titarev, E.F. Toro, WENO schemes based on upwind and centred TVD fluxes, Comput. Fluids 34 (2005) 705–720.
[33] E. Toro, Rieman Solvers and Numerical Methods for Fluid Dynamics, Springer, Berlin, Heidelberg, 1997.
[34] Q.H. Tran, B. Scheurer, High-order monotonicity-preserving compact schemes for linear scalar advection on 2-D irregular meshes, J. Comput. Phys. 175 (2002) 454–486.
[35] B. Van Leer, Towards the ultimate conservative difference scheme. V. A second-order sequel to Godunov's method, J. Comput. Phys. 32 (1979) 101–136.
[36] P. Woodward, P. Colella, The numerical simulation of two-dimensional fluid flow with strong shocks, J. Comput. Phys. 54 (1984) 115–173.